Posted on 28 May 2024 — The copyright holder is the author/funder. All rights reserved. No reuse without permission. — https://doi.org/10.22541/essoar.171136789.97903438/v2 — This is a preprint and has not been peer-reviewed. Data may be preliminary.

Estimating the Electric Fields Driving Lightning Dart Leader Development with BIMAP-3D Observations

Daniel Jensen[1], Xuan-Min Shao[1], Richard Sonnenfeld[2], and Caitano daSilva[3]

[1]Los Alamos National Laboratory
[2]New Mexico Tech
[3]New Mexico Institute of Mining & Technology

December 03, 2024

Abstract

In this paper, a numerical dart leader model has been implemented to understand the leader's development and the corresponding electric field changes observed by the 3D Broadband Mapping And Polarization (BIMAP-3D) system. The model assumes the extending leader channel is equipotential and has a linear charge distribution induced by an ambient electric field. The charge distribution induced by the ambient field can be used to model the electric field change at the ground. We then find the ambient electric field which best fits the field change measurements at the two BIMAP stations. The estimated ambient electric field decreases in the direction of dart leader propagation. Our observations and modeling results are consistent with our earlier hypothesis that dart leader speed is proportional to the electric field at the leader tip. The model also supports our earlier analysis that leader speed variations near branch junctions were due to previous charge deposits near the junctions. The modeled tip electric field is generally lower than the breakdown field unless the pre-dart-leader channel has a significant temperature of ˜3000 K. This is consistent with the fact that dart leaders typically do not form new branches into the virgin air. Furthermore, the tip field is generally close to the negative streamer stability field at ambient temperatures, explaining the nature of the narrow and well-defined channel structure. In addition to the charge distribution and the ambient and tip electric field, the development of the channel potential and current distribution are also presented.

Supporting Information for

Estimating the Electric Fields Driving Lightning Dart Leader Development with BIMAP-3D Observations

Daniel P. Jensen [1,2], Xuan-Min Shao [1], Richard G. Sonnenfeld [2], and Caitano L. da Silva [2]

[1]Electromagnetic Sciences & Cognitive Space Applications, Los Alamos National Laboratory, Los Alamos, NM, USA

[2]Langmuir Laboratory for Atmospheric Research, New Mexico Institute of Mining and Technology, Socorro, NM, USA

Contents of this file

1. Figures S2 to S15

Introduction

This document contains additional figures to support and expand our conclusions from the main text.

Figure S1 shows the results for dart leader K-5 with polynomial order $n = 50$, in the format of Figure 4 in the main text, as an illustration of what happens when the degrees of freedom are not constrained. The fits to the fast antenna measurements are not noticeably improved compared to the low order polynomials in the main text ($n = 1$, $n = 2$), while the ambient field displays an unreasonable amount of variation over relatively short distances.

Figures S2 and S3 show results when applying an internal potential gradient to the channel rather than assuming a perfect equipotential. Figure S2 is in the format of Figure 4 in the main text, while Figure S3 is in the format of Figure 6 from the main text.

Figures S4 and S5 show results when assuming dart leader K-5 extends bidirectionally. The modeled leader channel starts between s=-100 m and s=0 m at time t=0, then it extends at equal speeds in both the $-\hat{s}$ and $+\hat{s}$ directions. The path in the $-\hat{s}$ direction (positive tip) follows the branch as observed by VHF earlier in the flash, in the direction away from the flash origin. The positive tip stops propagating once it has reached the previously observed end of the branch. The negative tip propagation matches the observed VHF dart leader development. Figure S4 is in the format of Figure 4 in the main text, while Figure S5 is in the format of Figure 6 from the main text. Figure S4 includes the tip field and potential drop for both the negative and positive tips of the dart leader.

The remaining Figures (S6 through S15) show the results of applying our equipotential methodology to additional dart leaders from the same flash. For these dart leaders we are explicitly looking for an ambient field solution which matches both the measured field change and the measured leader speed. This is done by including the χ^2_{speed} term from Equation 22 in the main text. The μ value ($v = \mu E_{tip}$) is determined as the median value of $v(t)/E_{\text{tip}}(t_k)$ for each iteration. These figures are included to give a broader view of our results, both with cases that generally support our conclusions from the main text, and a few examples where we were not able to fit the observed field changes. Figures S6 through S15 are all in the format of Figure 4 from the main text. For some of these additional dart leaders, especially K-2 (Figure S7), significant bidirectional development is added in order to improve the fit to the fast antenna measurements. Bidirectional development is noted in the figure captions, and can also be noted by large negative values of channel distance. In each case we used the smallest amount of bidirectional development that allowed for a reasonable fit.

Copyright 2024 by the American Geophysical Union.
0148-0227/24/$9.00

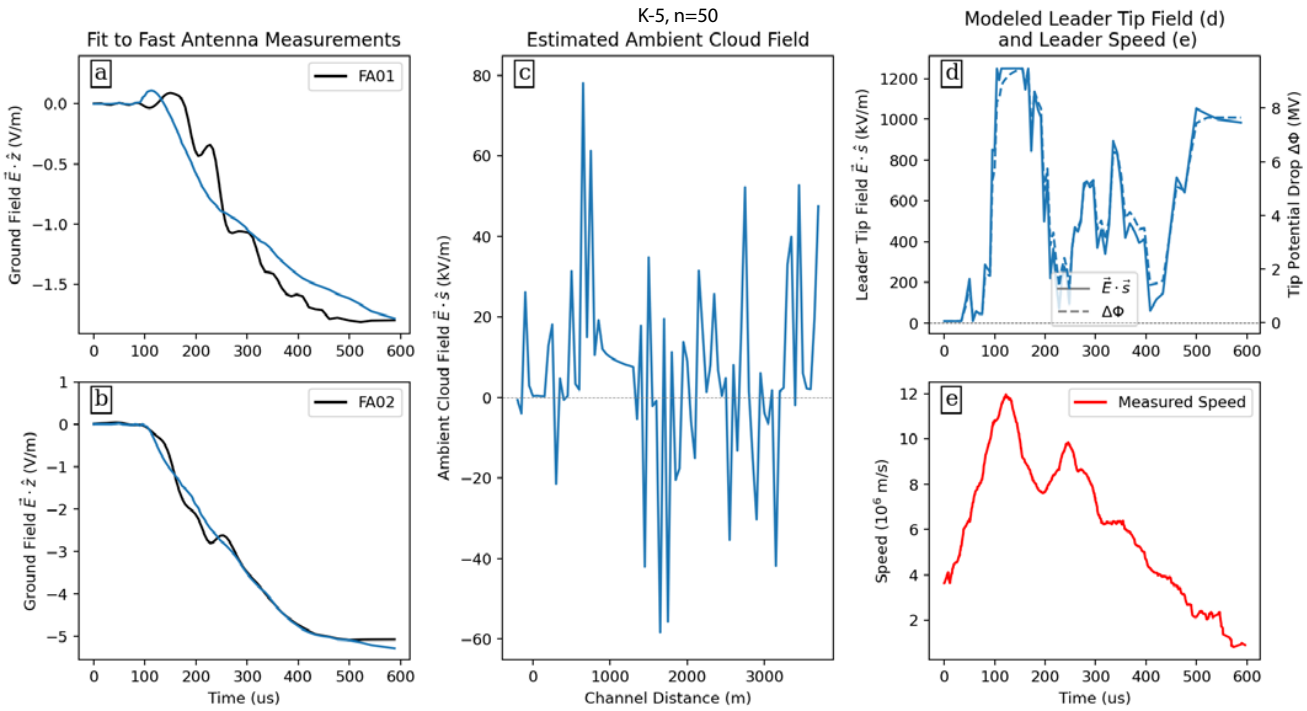

Figure S1. Field results for dart leader K-5 for n=50. Plots show the measured and modeled field change vs time for FA01 (a) and FA02 (b), the estimated ambient field vs channel distance (c), the modeled tip field and tip potential drop vs time (d), and the measured leader speed vs time (e). The fit to the fast antenna data is not significantly improved despite the massive increase in degrees of freedom, while the estimated ambient field varies an unreasonable amount over short distances.

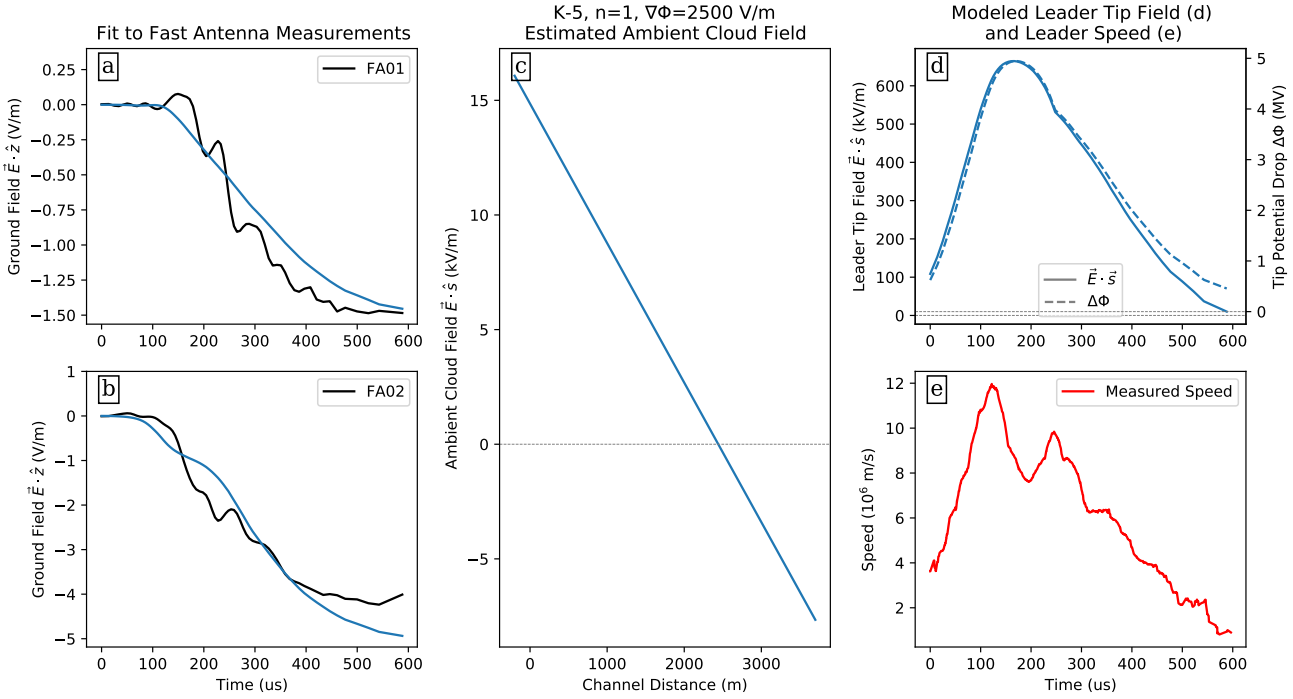

Figure S2. Field results for dart leader K-5 in the n=1 case when including an internal potential gradient of 2.5 kV/m. Plots show the measured and modeled field change vs time for FA01 (a) and FA02 (b), the estimated ambient field vs channel distance (c), the modeled tip field and tip potential drop vs time (d), and the measured leader speed vs time (e).

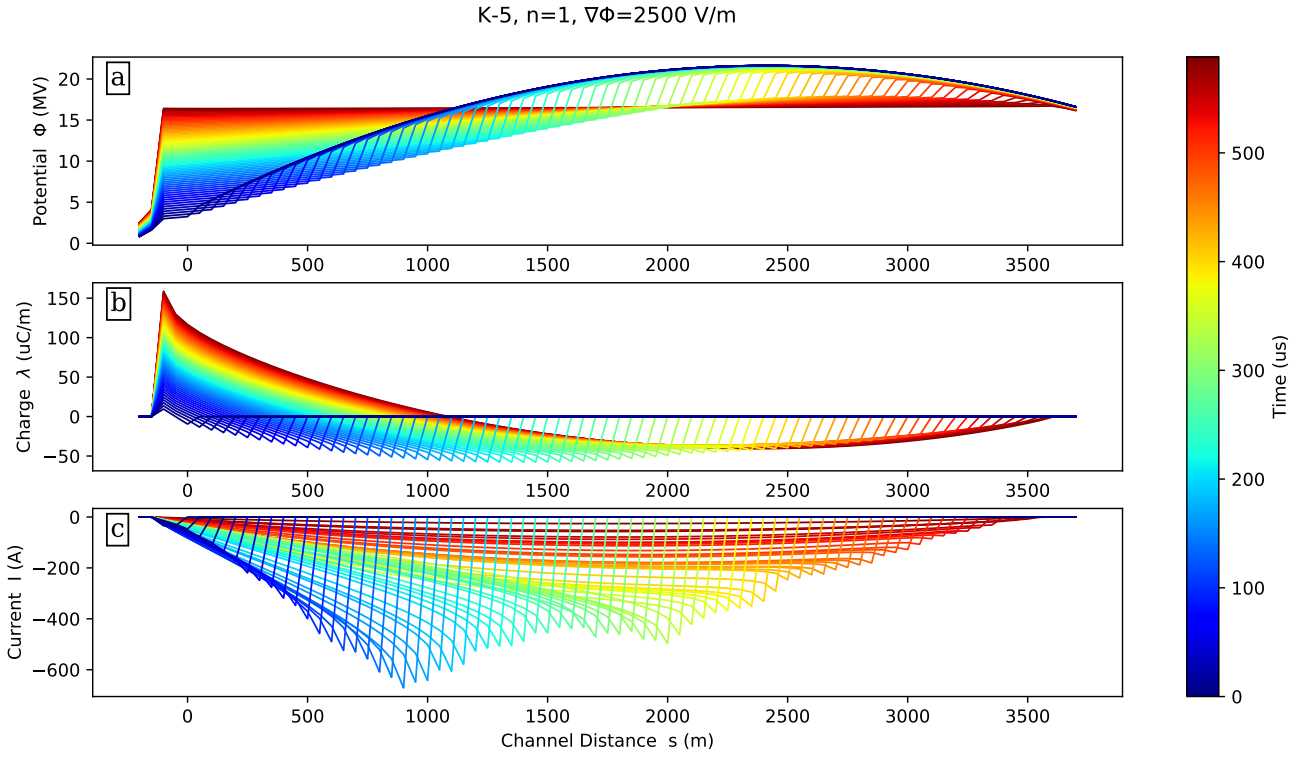

Figure S3. Modeling results for dart leader K-5 in the n=1 case when including an internal potential gradient of 2.5 kV/m. Plots show the potential distribution (a), charge distribution (b), and current distribution (c), all plotted vs channel distance and colored by time.

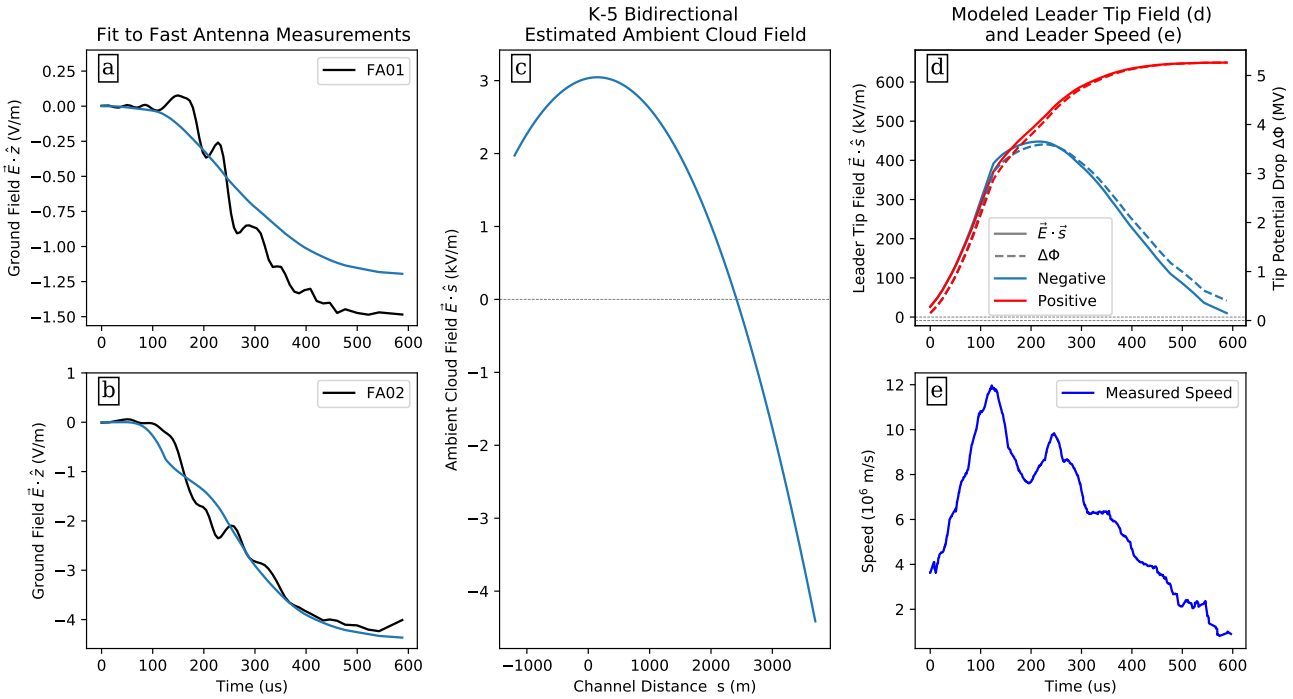

Figure S4. Field results for dart leader K-5 in the n=2 case when including bidirectional development. Plots show the measured and modeled field change vs time for FA01 (a) and FA02 (b), the estimated ambient field vs channel distance (c), the modeled tip field and tip potential drop vs time for the negative (blue) and positive (red) tips of the dart leader (d), and the measured leader speed vs time (e). Negative channel distance indicates extension of the positive tip in the direction away from the flash origin. The positive tip starts at s=-100 m and the negative tip starts at s=0 m.

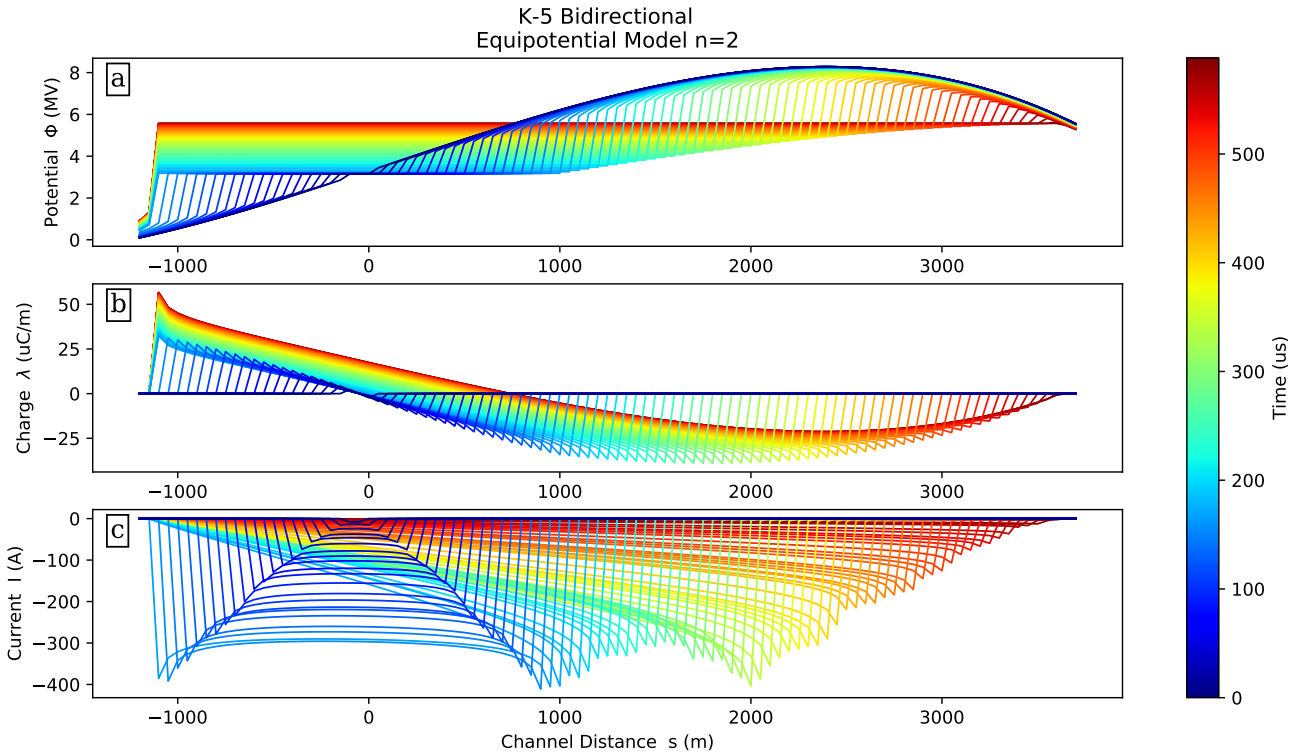

Figure S5. Modeling results for dart leader K-5 in the n=2 case when including bidirectional development. Plots show the potential distribution (a), charge distribution (b), and current distribution (c), all plotted vs channel distance and colored by time. Negative channel distance indicates extension of the positive tip in the direction away from the flash origin. The positive tip starts at s=-100 m and the negative tip starts at s=0 m.

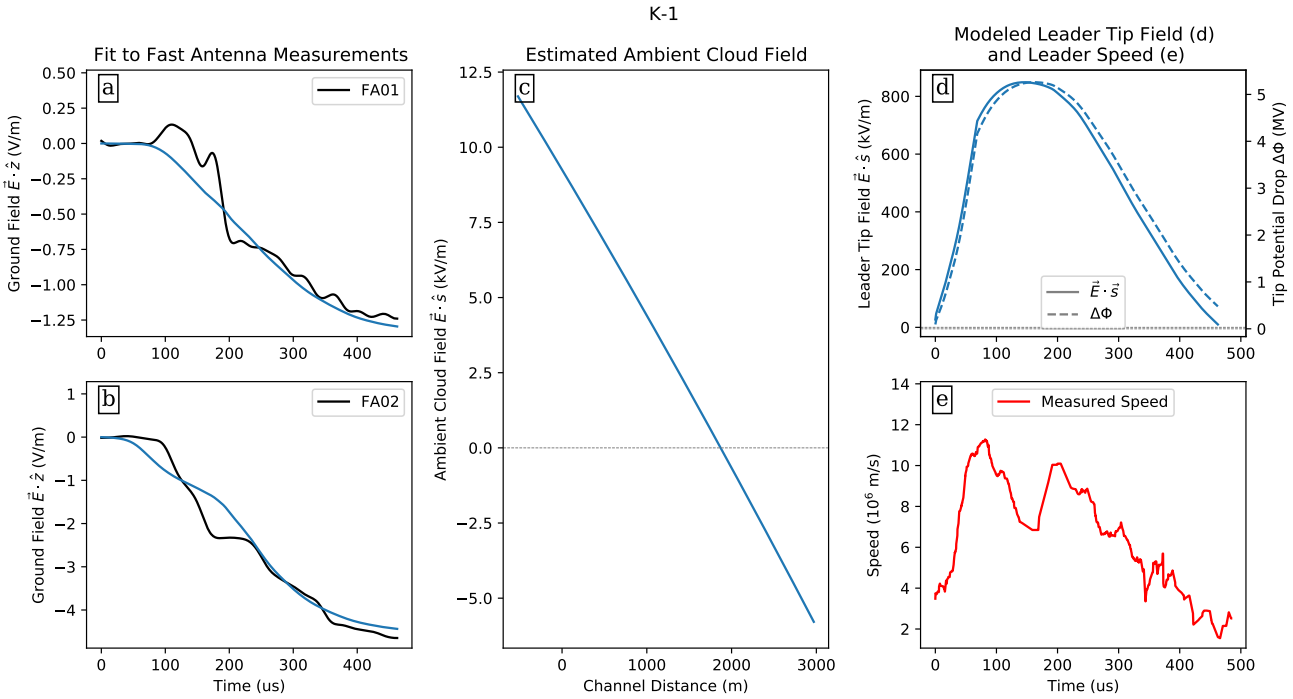

Figure S6. Results for dart leader K-1 with an equipotential channel. Plots show the measured and modeled field change vs time for FA01 (a) and FA02 (b), the estimated ambient field vs channel distance (c), the modeled tip field and tip potential drop vs time (d), and the measured leader speed vs time (e). The modeled leader includes a 500 m extension of the positive tip to improve the field change and speed fit. The model matches the field change and speed fairly well.

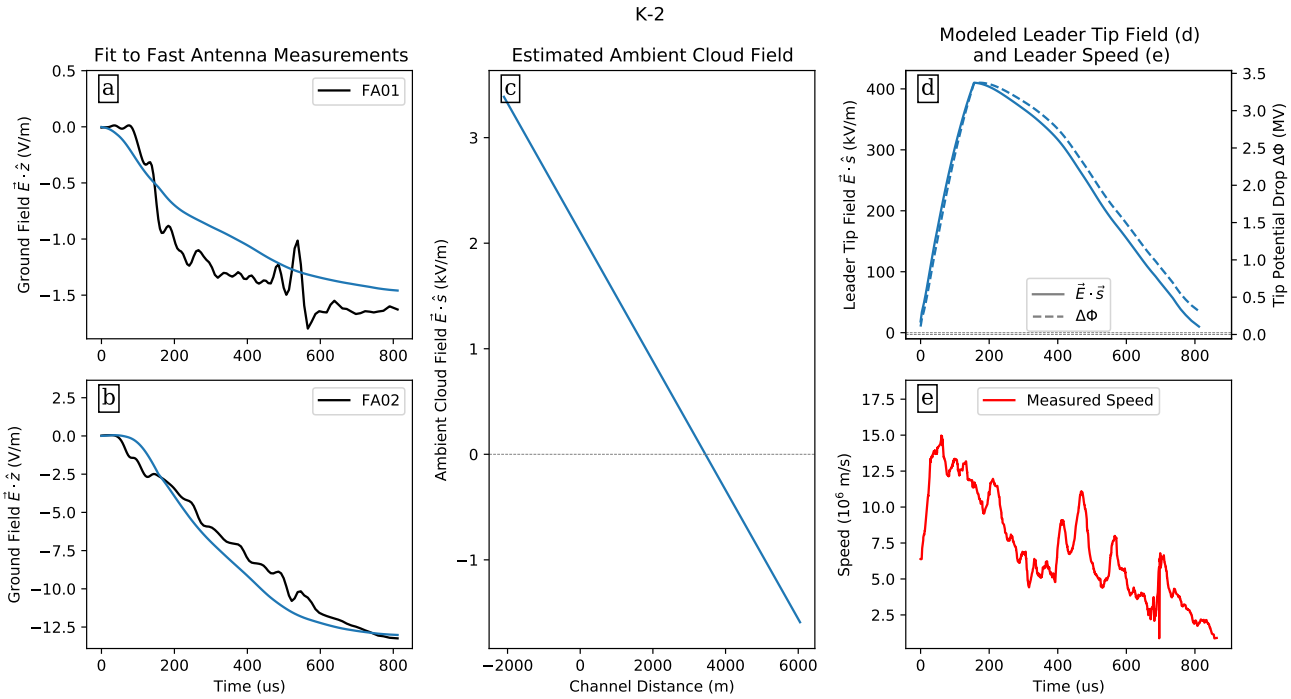

Figure S7. Results for dart leader K-2 with an equipotential channel. Plots show the measured and modeled field change vs time for FA01 (a) and FA02 (b), the estimated ambient field vs channel distance (c), the modeled tip field and tip potential drop vs time (d), and the measured leader speed vs time (e). The modeled leader includes a 2000 m extension of the positive tip, without this the field changes at FA01 and FA02 cannot be fit simultaneously. The model fits the field changes fairly well, and the tip field is at least somewhat correlated with the leader speed.

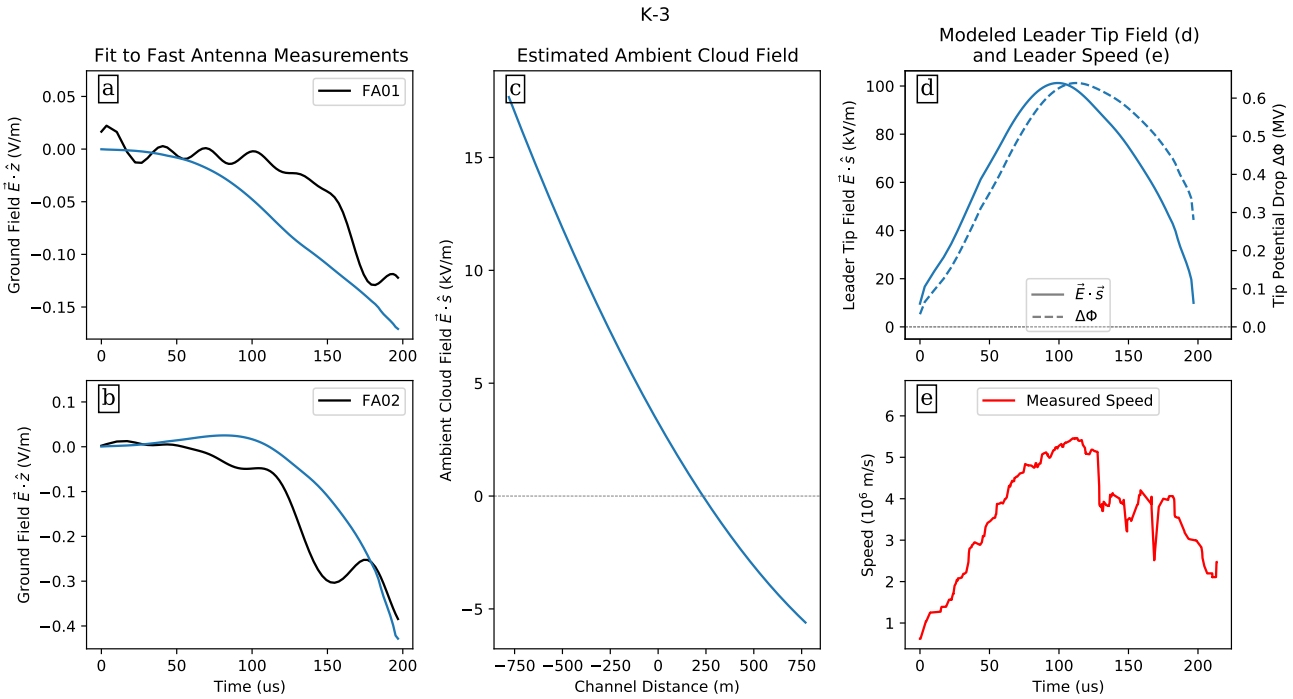

Figure S8. Results for dart leader K-3 with an equipotential channel. Plots show the measured and modeled field change vs time for FA01 (a) and FA02 (b), the estimated ambient field vs channel distance (c), the modeled tip field and tip potential drop vs time (d), and the measured leader speed vs time (e). The modeled leader does not include significant extension of the positive tip. Considering that the field change is small relative to the noise level the model fits fairly well, and there is a general correlation between the tip field and speed.

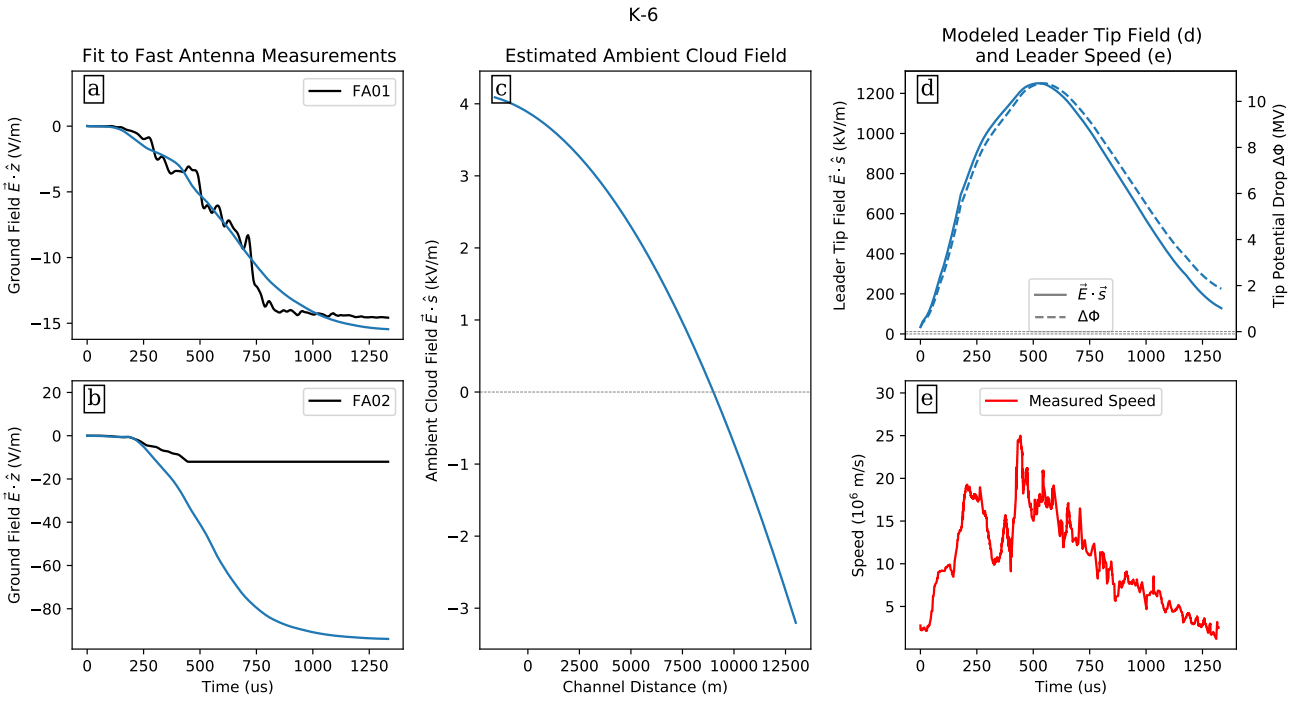

Figure S9. Results for dart leader K-6 with an equipotential channel. Plots show the measured and modeled field change vs time for FA01 (a) and FA02 (b), the estimated ambient field vs channel distance (c), the modeled tip field and tip potential drop vs time (d), and the measured leader speed vs time (e). The modeled leader does include a 1500 m extension of the positive tip in order to improve the tip field correlation with the speed. The field change at FA02 saturated the sensor, so the saturated portions are not included in the χ^2 fit. Even in the unsaturated portions between 250 μs and 500 μs the measured field change is much smaller than the modeled change, but it is difficult to properly constrain the results without a longer record to compare to. The tip field that results from matching FA01 does generally correlate with the speed, other than the branch junction variations.

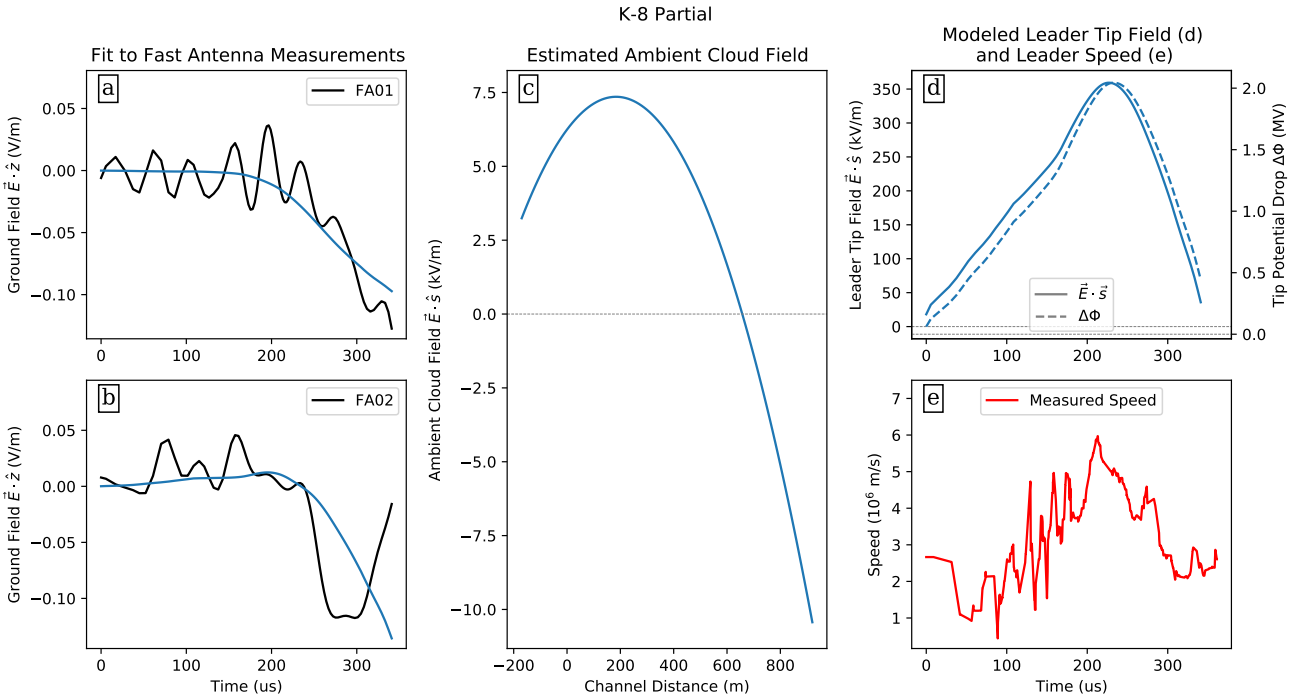

Figure S10. Results for the initial part of dart leader K-8, up to the first junction, with an equipotential channel. Plots show the measured and modeled field change vs time for FA01 (a) and FA02 (b), the estimated ambient field vs channel distance (c), the modeled tip field and tip potential drop vs time (d), and the measured leader speed vs time (e). The modeled leader does not include any significant extension of the positive tip. The net electrostatic field change is fairly small compared to the noise, but the fit to the field change and leader speed is fairly good for this portion of the leader.

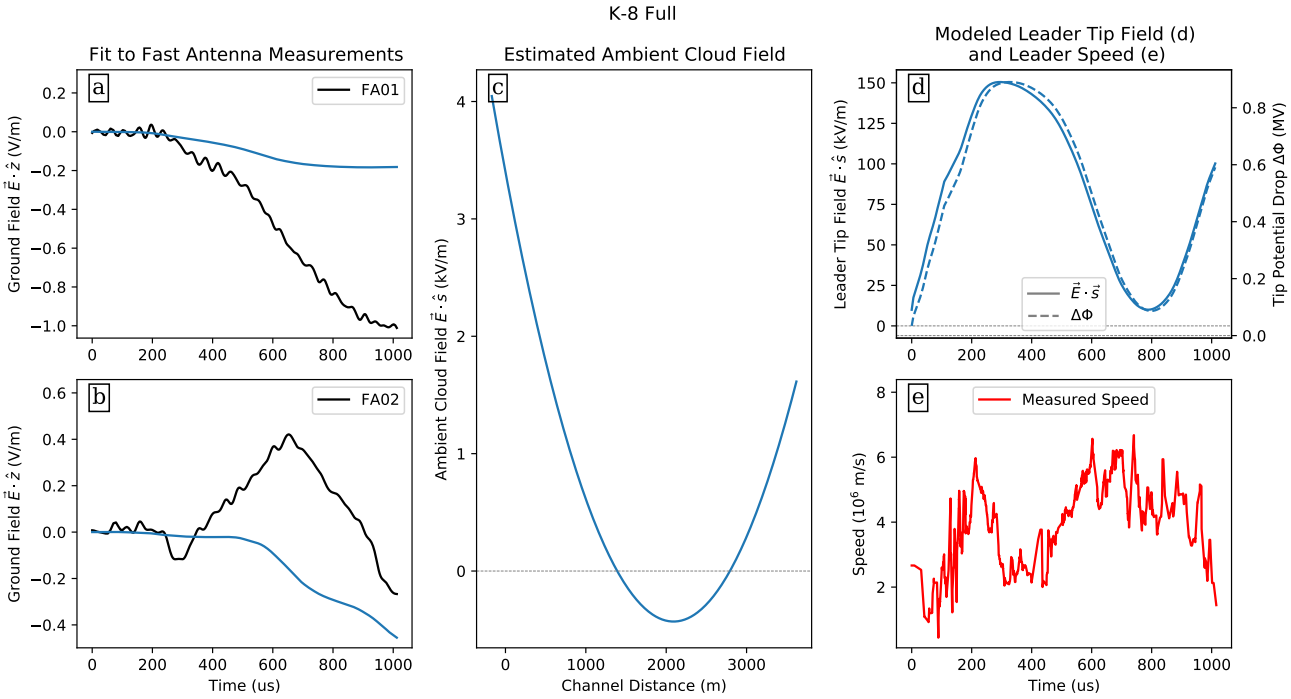

Figure S11. Results for the full development of dart leader K-8 with an equipotential channel. Plots show the measured and modeled field change vs time for FA01 (a) and FA02 (b), the estimated ambient field vs channel distance (c), the modeled tip field and tip potential drop vs time (d), and the measured leader speed vs time (e). The modeled leader does not include any significant extension of the positive tip. After the first junction around 300 μs FA02 measured a positive field change while FA01 continues to change in the negative direction, we were not able to match both of these field changes simultaneously. The tip field also does not match the measured speed well, but with such a poor fit to the field changes it is clear the model is not valid for the full leader development in this case, possibly due to conductivity extending down the other branch at the first junction. Otherwise it is not clear why the field changes are so different for this dart leader.

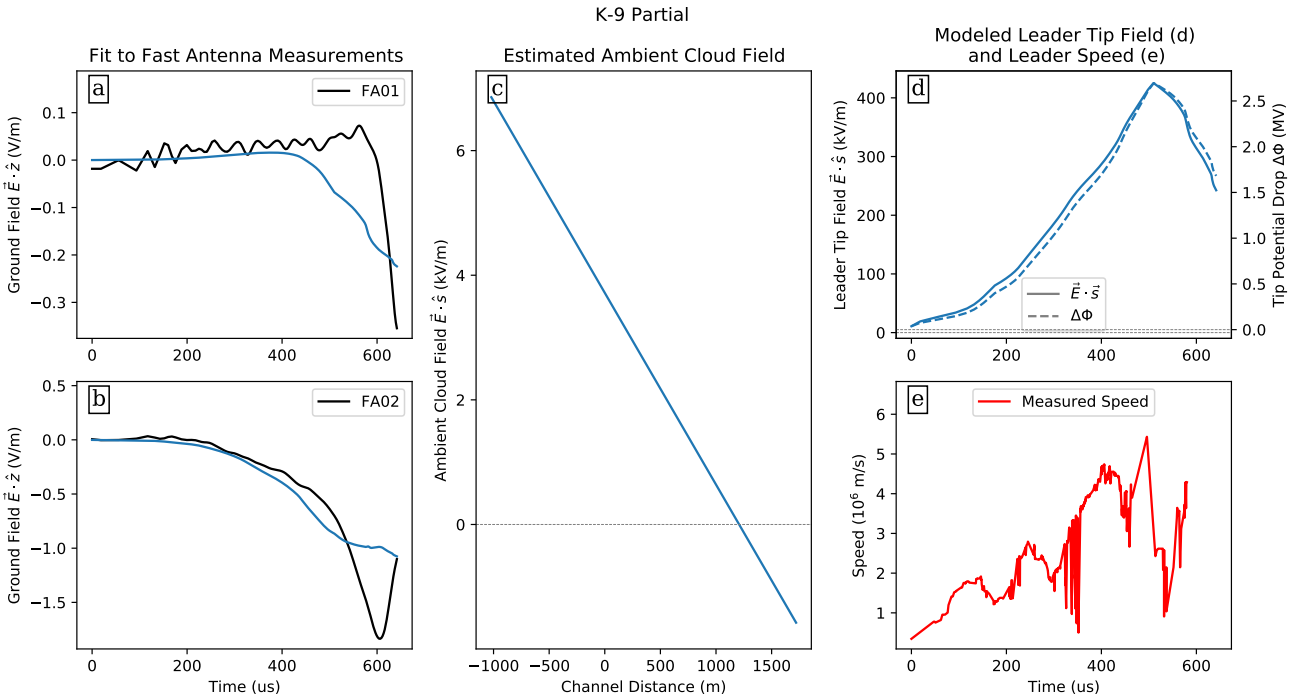

Figure S12. Results for the initial part of dart leader K-9, before it splits into multiple branches, with an equipotential channel. Plots show the measured and modeled field change vs time for FA01 (a) and FA02 (b), the estimated ambient field vs channel distance (c), the modeled tip field and tip potential drop vs time (d), and the measured leader speed vs time (e). The modeled leader does include a 1000 m extension of the positive tip in order to improve the fit to the FA02 field change. Both field changes show a sudden change around 600 μs, probably related to the other branches starting to develop. The tip field is well correlated with the general trend of the leader speed.

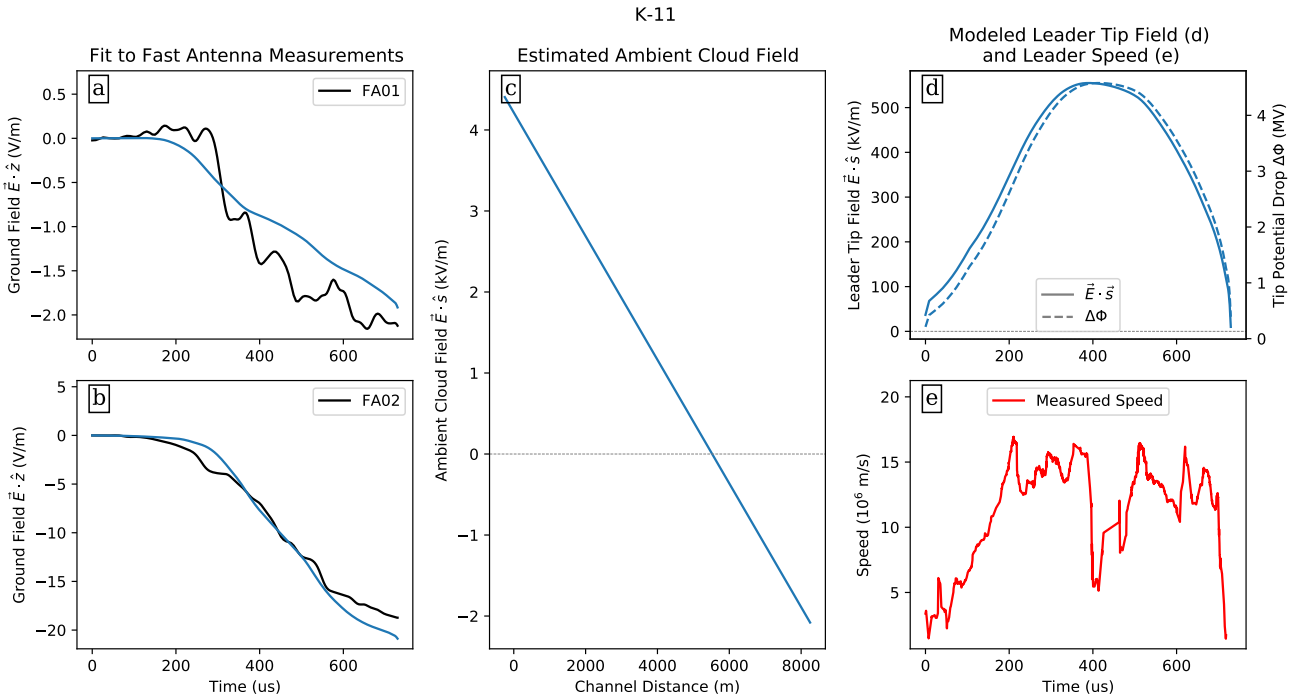

Figure S13. Results for dart leader K-11 with an equipotential channel. Plots show the measured and modeled field change vs time for FA01 (a) and FA02 (b), the estimated ambient field vs channel distance (c), the modeled tip field and tip potential drop vs time (d), and the measured leader speed vs time (e). The modeled leader does not have any significant extension of the positive tip. The fit to the field changes is fairly good, and the modeled tip field is somewhat correlated to the measured speed.

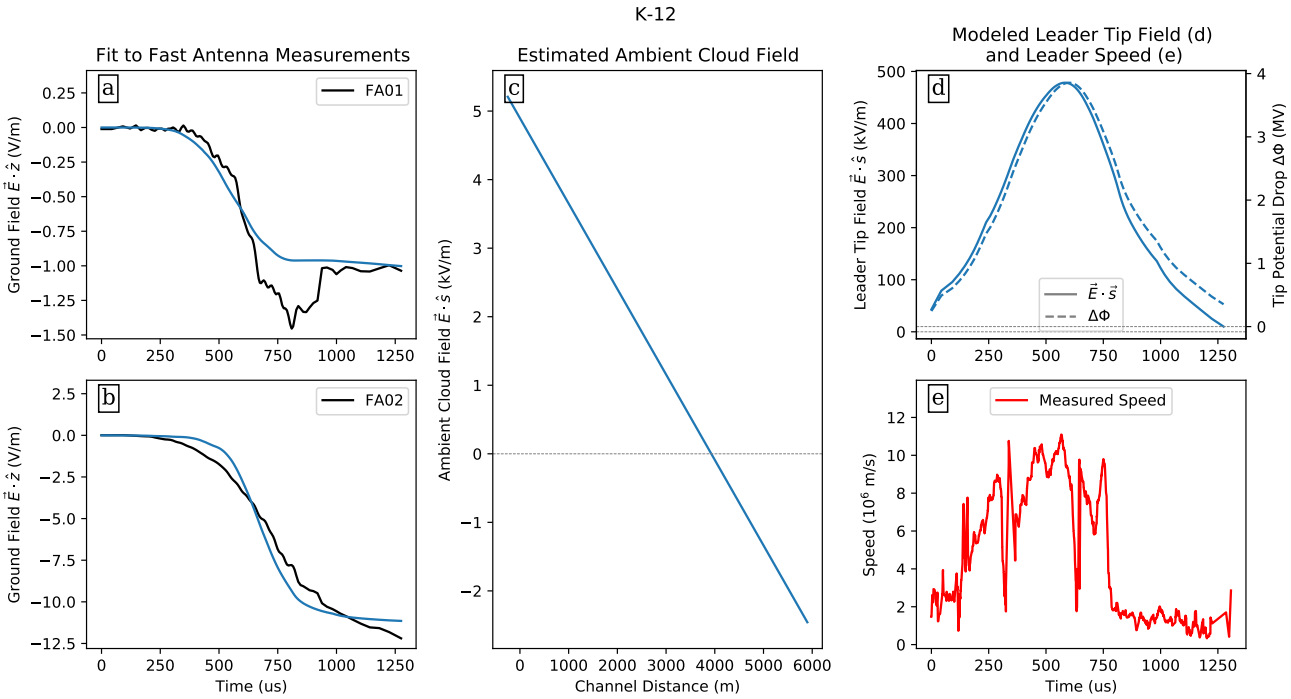

Figure S14. Results for dart leader K-12, with an equipotential channel. Plots show the measured and modeled field change vs time for FA01 (a) and FA02 (b), the estimated ambient field vs channel distance (c), the modeled tip field and tip potential drop vs time (d), and the measured leader speed vs time (e). The modeled leader does not have any significant extension of the positive tip. The fit to the field changes is fairly good, except the temporary deviation of FA01 around 750 μs, and the modeled tip field is somewhat correlated to the measured speed.

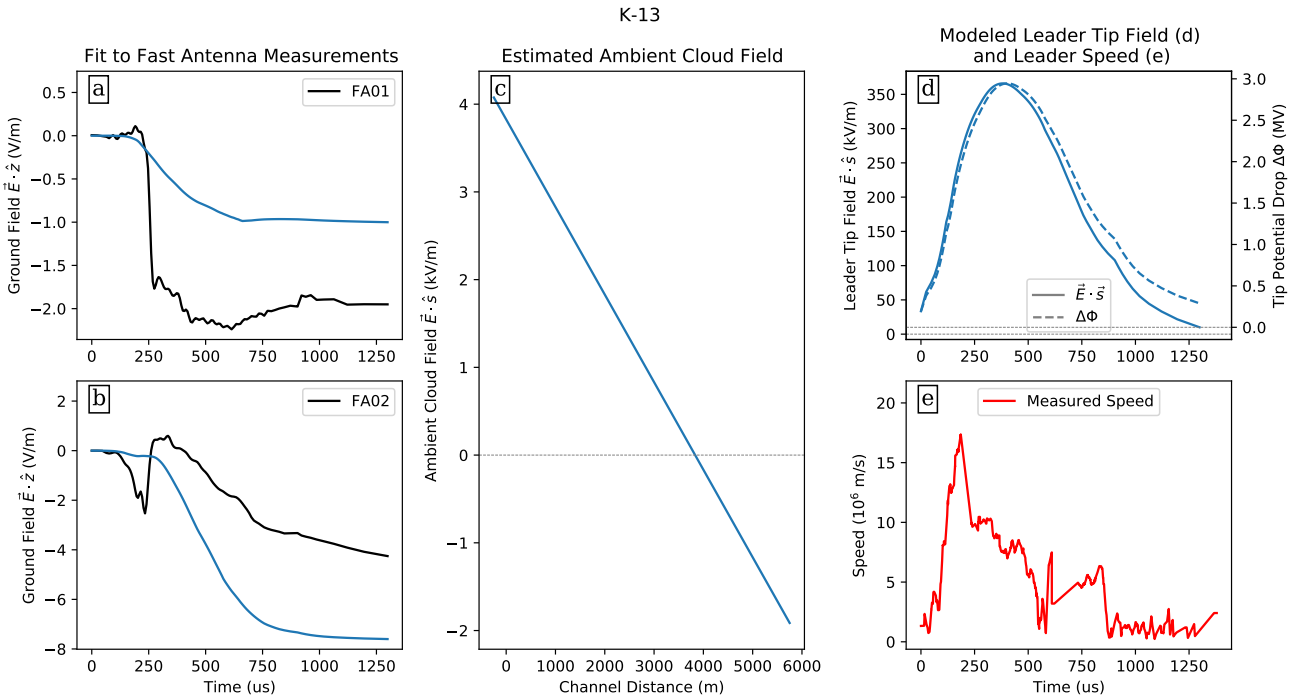

Figure S15. Results for dart leader K-13, with an equipotential channel. Plots show the measured and modeled field change vs time for FA01 (a) and FA02 (b), the estimated ambient field vs channel distance (c), the modeled tip field and tip potential drop vs time (d), and the measured leader speed vs time (e). The modeled leader does not have any significant extension of the positive tip. We were not able to simultaneously fit both the FA01 and FA02 field changes, possibly due to conductivity extending down the other branch at the first junction. Since the model does not fit the measured field changes the rest of the model results are clearly not valid.

Estimating the Electric Fields Driving Lightning Dart Leader Development with BIMAP-3D Observations

Daniel P. Jensen [1,2], Xuan-Min Shao [1], Richard G. Sonnenfeld [2], and Caitano L. da Silva [2]

[1]Electromagnetic Sciences & Cognitive Space Applications, Los Alamos National Laboratory, Los Alamos, NM, USA
[2]Langmuir Laboratory for Atmospheric Research, New Mexico Institute of Mining and Technology, Socorro, NM, USA

Key Points:

- We estimate cloud ambient electric fields by combining 3D mapping and electric field change observations with an equipotential leader model
- Our results are consistent with the hypothesis that dart leader speed is proportional to the leader tip electric field
- The modeled tip fields also explain why dart leaders typically follow previous channels and appear narrow in VHF compared to step leaders

Corresponding author: Daniel Jensen, dpjensen@lanl.gov

Abstract

In this paper, a numerical dart leader model has been implemented to understand the leader's development and the corresponding electric field changes observed by the 3D Broadband Mapping And Polarization (BIMAP-3D) system. The model assumes the extending leader channel is equipotential and has a linear charge distribution induced by an ambient electric field. The charge distribution induced by the ambient field can be used to model the electric field change at the ground. We then find the ambient electric field which best fits the field change measurements at the two BIMAP stations. The estimated ambient electric field decreases in the direction of dart leader propagation. Our observations and modeling results are consistent with our earlier hypothesis that dart leader speed is proportional to the electric field at the leader tip. The model also supports our earlier analysis that leader speed variations near branch junctions were due to previous charge deposits near the junctions. The modeled tip electric field is generally lower than the breakdown field unless the pre-dart-leader channel has a significant temperature of ∼3000 K. This is consistent with the fact that dart leaders typically do not form new branches into the virgin air. Furthermore, the tip field is generally close to the negative streamer stability field at ambient temperatures, explaining the nature of the narrow and well-defined channel structure. In addition to the charge distribution and the ambient and tip electric field, the development of the channel potential and current distribution are also presented.

Plain Language Summary

A dart leader is a discharge process that occurs at the later stage of a lightning flash. It retraces the path established by earlier discharges and propagates at a high speeds of 1%-10% the speed of light. Recently we developed a system called BIMAP-3D that can map lightning radio sources in 3D with high time resolution. We also measured the electric field at the ground caused by lightning discharges. In this paper we modeled a 3D mapped dart leader as a perfectly conducting wire. A conducting wire placed in an external electric field disturbs the field around it. We used our wire dart leader model to find an electric field in the cloud so that the modeled disturbance matched the electric fields we measured at the ground. The estimated cloud field decreases in the direction of dart leader propagation. Our model suggests that the speed of a dart leader is closely related to electric field at the dart leader tip. The modeled electric field at the dart leader tip is also too low to form a new discharge path through the air, explaining why they follow previously established paths.

1 Introduction

In Jensen et al. (2023b) we analyzed 14 in-cloud dart leaders (also called K-leaders or recoil leaders) with 3D Broadband Interferometeric Mapping And Polarization (BIMAP-3D) observations. The dart leaders often exhibited an overall initial acceleration and a gradual deceleration, and some rapid speed variations as the leaders passed branch junctions in the flash structure. We proposed that the dart leader speed was proportional to the electric field strength at the leader tip when the leader is considered an equipotential channel growing through an ambient electric field. Based on the overall speed trend, it was inferred that the ambient electric field decreases in the direction of the leader propagation. We also used a simple two-point dipole charge model to estimate the development of the charge distribution along the leader channel based on the field change measured by two fast electric field change antennas. This paper expands on the work of Jensen et al. (2023b) by numerically modeling the development of equipotential dart leader channels constrained by our BIMAP-3D and fast antenna observations.

The leader model used in this study was first suggested by Kasemir (1960), who applied the basic concepts of electrostatics to approximate conductive lightning chan-

nels as equipotential and growing in an electric field, with qualitative descriptions of the induced charge distribution. Mazur and Ruhnke (1993, 1998) expanded upon Kasemir's initial work with numerical modeling of equipotential lightning channels. The model of Kasemir (1960) has historically been referred to as the bidirectional leader model, we will instead refer to it as the equipotential leader model, since the equipotential assumption is the most significant difference between this model and other non-physics-based leader models. A number of studies have used measured field changes to model simple charge configurations along leader channels without considering leader conductivity (Cai et al., 2022; Chen et al., 2013; Gao et al., 2020; Jensen et al., 2023b; Karunarathne et al., 2015; Lu et al., 2011). By contrast, relatively few studies have attempted to compare the equipotential model to observed electric field changes associated with lightning (Mazur & Ruhnke, 1993; Pasko, 2014; da Silva & Pasko, 2015), and these studies have been somewhat limited by lack of knowledge of the extent or location of the leader channel.

The BIMAP-3D system has the capability to map out very high frequency (VHF) radio sources along lightning channels in 3D over time (Shao et al., 2023), and simultaneously measures the electric field changes with a fast antenna at each of the two BIMAP stations. If we assume the active and continuous dart leader channel sections with recent VHF activity are at equipotential, and choose some reasonable channel radius, the only remaining unknown in the model is the cloud electric field distribution along the channel. The cloud electric field can then be estimated through standard non-linear inverse problem techniques as described in Section 3.

This approach to indirectly measuring the ambient electric field is similar in concept to the work reported by Cummer (2020), but our use of time resolved leader lengths and field changes allows the estimated ambient field along the leader channel to be spatially resolved. This additional information leads to a number of insights on the physical conditions of the developing channel.

As a note on terminology, in our previous papers (Jensen et al., 2021, 2023b) we have discussed the use of the terms "K-leader", "dart leader", and "recoil leader" to refer to what is fundamentally the same phenomenon. Following some recent discussion and consensus within at least part of the lightning community (Hare et al., 2023b, 2024; Kolmašová et al., 2023; da Silva et al., 2023) we now choose to use the term dart leader exclusively to refer to this phenomenon, as we previously suggested in Jensen et al. (2021). To avoid confusion about whether a dart leader is followed by a return stroke we suggest that dart leaders may be further classified as in-cloud (IC) dart leaders or cloud-to-ground (CG) dart leaders whenever the distinction is relevant, as we suggested in Jensen et al. (2021).

Following this terminology convention, in this paper we apply the equipotential model to IC dart leaders to understand the electric fields and other conditions that drive the leader's development. This work builds on recently reported observations of dart leaders (Jensen et al., 2023b), and serves as a more rigorous test of some of our hypotheses on the dart leader propagation physics. When applying the methodology discussed in Section 3 the model results are consistent with our hypothesis that dart leader speed is proportional to the leader tip electric field, as we first suggested in Jensen et al. (2021). We demonstrate that an ambient field which starts relatively high and decreases along the channel results in a tip field that matches the observed speed trends of initial acceleration and gradual deceleration. We also confirm that the branch junction speed variations can be explained by charge deposits near the primary channel. Our results also provide possible explanations to some other observed dart leader properties, such as their well-defined and narrow channel width in VHF and the fact that they typically do not exit the pre-conditioned channel structure to propagate through virgin air.

2 Instrumentation

In this paper we make use of lightning observations from the BIMAP-3D system (Shao et al., 2023) that has been deployed at Los Alamos National Laboratory (LANL) since 2021. It consists of two stations, each with four VHF antennas arranged in a Y configuration. The two stations are 11.5 km apart. Lightning data from each station is first processed separately to form a 2D lightning map, and then is combined and reprocessed to produce a 3D lighting map. Based on observations of dart leader channel widths, the random uncertainty of BIMAP-3D can be better than 10 m in easting, northing, and altitude in ideal conditions (Shao et al., 2023). Systematic biases in the absolute location have not been evaluated, but the 3D results produced by the triangulation and DTOA location techniques typically differ by less than 30-50 m, and this gives an estimate of the absolute location error. For lightning channels several kilometers away a location bias of 50 m is negligible for this study.

BIMAP-3D also has a fast electric field change antenna, or fast antenna (FA) at each station. We are using fast antennas previously developed for the Los Alamos Sferics Array (LASA) (Smith et al., 2002) to measure vertical electric fields at the ground. The fast antenna at station 1 (FA01) has a highpass time constant of 1 ms, and the fast antenna at station 2 (FA02) has a time constant of 0.2 ms. For a first order highpass filter the low frequency content can be reliably recovered by de-drooping (deconvolution) (Födisch et al., 2016; Sonnenfeld et al., 2006) as long as the low frequency signal is sufficiently above the noise level, the direct current (DC) offset or "zero-level" of the signal is reliably known, and the signal does not saturate. For both FA01 and FA02 the low frequency content can be recovered down to the 60 Hz noise from nearby power infrastructure. There is no explicit lowpass filter in the fast antennas, but above 20 MHz there is essentially no signal. In this study we are interested in the electrostatic field change associated with the dart leaders, so we digitally lowpass the signals at 25 kHz. The flash being analyzed occurs close enough that the measured field change is essentially all electrostatic. The field change signals we are analyzing are thus more in the slow antenna regime (Zhang, 2010, page 8). We also de-droop the field change for each dart leader separately, making use of the fact that there is essentially no field change in the interval between dart leaders for this flash. In addition to recovering the low frequency content, de-drooping corrects for any differences caused by the different time constants between the two fast antennas.

In Jensen et al. (2023b) we found a relative calibration between FA01 and FA02 by comparing peak amplitudes for distant return strokes. This relative calibration was sufficient for qualitative modeling analysis. For quantitative modeling in this paper, we need an absolute calibration for each fast antenna. To achieve this we used 48 hours of National Lightning Detection Network (NLDN) peak current data for strikes within 100 km of our stations that were captured by either of our stations. We restricted the NLDN data set to strikes that were at least 15 km away from both stations, and with reported peak currents between 0 kA and -50 kA. With these restrictions we found 263 strikes for FA01 and 87 strikes for FA02. To compare NLDN peak currents to our field change measurements we used the empirical relation of Equation 4 in Nag et al. (2014) (first reported by Rakov et al. (1992) based on results from Willett et al. (1989)). Based on this equation we derived calibration factors for our fast antennas based on each NLDN strike, with units of $\left[\frac{V}{m}\right]$ per digital count. After finding the calibration factor for each match between the NLDN and our fast antennas, and removing any obvious outliers, we found the average calibration factor for each station. The calibration factors were 4±2 mV/(m·count) for FA01 and 2±1 mV/(m·count) for FA02. In each case the 1σ uncertainties are about 50% of the calibration value. This is a significant source of uncertainty for all the quantities calculated in this paper.

3 Methods

3.1 The Equipotential Leader Model

Following the approach of Mazur and Ruhnke (1998), we consider a leader as a long cylinder with effective capacitive radius r_C. If the cylindrical channel is placed in an ambient potential distribution $\Phi_{amb}(s)$ and a linear charge distribution $\lambda(s)$ is placed along the channel, then the new potential along the channel $\Phi(s)$ will be given by:

$$\Phi(s) = \Phi_{amb}(s) + \frac{1}{4\pi\varepsilon_0}\int_{s_a}^{s_b} \frac{\lambda(s')ds'}{\sqrt{(s-s')^2 + r_C^2}} \tag{1}$$

where s is the coordinate along the length of the channel. s_a and s_b are the ends of the channel.

For an assumed equipotential channel we have $\Phi(s) = \Phi_{cha} = const.$ for $s_a \leq s \leq s_b$. We further assume that the leader has no net charge, since the transfer of charge between the leader and the cloud should be negligible at dart leader time scales. Under these assumptions the channel potential must be given by the average value (Mazur et al., 1995):

$$\Phi_{cha} = \frac{1}{s_b - s_a}\int_{s_a}^{s_b} \Phi_{amb}(s)ds \tag{2}$$

We then wish to find the charge distribution $\lambda(s)$ which satisfies this condition. To evaluate this numerically with the method of moments technique we discretize the leader channel into N segments of length Δs, where each segment has a uniform charge density λ_i. We then linearize Equation 1 as (da Silva & Pasko, 2015):

$$[\Phi_i] = [\Phi_{amb,i}] + [K_{i,j}]\,[\lambda_j] \tag{3}$$

where Φ_i is the net potential at s_i, $\Phi_{amb,i}$ is the ambient potential at s_i, and $[K_{i,j}]\,[\lambda_j]$ gives the approximate potential at s_i due to the linear charge density λ_j at every location s_j along the channel. Φ_i, $\Phi_{amb,i}$, and λ_j are the elements of column matrices of size $N \times 1$, and $K_{i,j}$ are the elements of an $N \times N$ matrix defined as

$$K_{i,j} = \frac{1}{4\pi\varepsilon_0}\int_{s_j-\Delta s/2}^{s_j+\Delta s/2} \frac{ds'}{\sqrt{(s_i-s')^2 + r_C^2}} \tag{4}$$

where $K_{i,j}$ has units of meters per Farad.

The discretized charge distribution can then be obtained as:

$$[\lambda_j] = [K_{i,j}]^{-1}\,[\Phi_{amb,i} - \Phi_{cha}] \tag{5}$$

A simple diagram of the leader model is shown in Figure 1, similar to Figure 4 of da Silva and Pasko (2015). For the equipotential calculations the leader channel is assumed to be perfectly straight for simplicity. Since the potential of each segment depends most strongly on the nearest segments our model should be approximately valid as long as the channel is approximately straight over lengths of a few times Δs. Our model is the same as the leader models used by Mazur and Ruhnke (1998) and Pasko (2014), where those two models differ only in their choice of radius r_C.

We can then apply this model repeatedly with leaders of increasing length $L(t) = s_b(t) - s_a(t)$, in order to approximate $\lambda(s,t)$ for a growing leader channel. The time step at each point in time will be $\Delta t_k = \Delta s / v_k$, where v_k is the speed of the leader growth at time t_k.

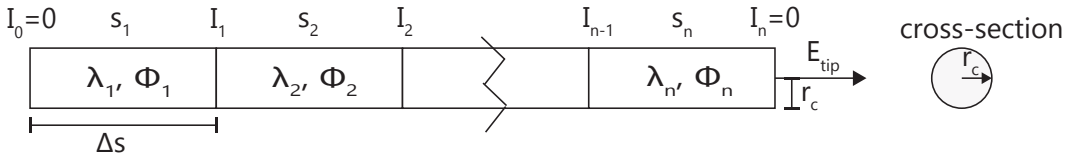

Figure 1. A diagram of the model setup with cylindrical segments of length Δs and radius r_C arranged end to end. Each cylinder has a linear charge density λ_i and potential Φ_i, and is centered at s_i. Current I_i is defined at the boundary between the s_{i+1} and s_i segments. A cross-section is shown on the right. The radius and length of segments are not drawn to scale. The axial tip electric field $E_{\rm tip}$ is also shown on the right edge of the n-th segment.

From the discrete charge distribution over time we can calculate the discretized current by solving the continuity equation for I_i as

$$I_i(t_k) = -\Delta s \sum_{j=1}^{i} \frac{\lambda_j(t_k) - \lambda_j(t_{k-1})}{t_k - t_{k-1}} \tag{6}$$

Calculation of the electric field at the leader tip $E_{\rm tip}$ is somewhat nuanced because of uncertainty about the effective channel radius r_C, so we will discuss this separately in Section 3.2.

The leader tip potential drop $\Delta\Phi_{\rm tip}$ can also be calculated, it is simply defined as

$$\Delta\Phi_{\rm tip} = \Phi_{cha} - \Phi_{amb}(s_{tip}) \tag{7}$$

This is the difference between the channel potential and the ambient potential that would exist at the tip if there was no leader present. Our $\Delta\Phi_{\rm tip}$ is similar to the definition of ΔU_g^* in Celestin and Pasko (2011), or ΔU_t in Bazelyan and Raizer (2000) (Equation 4.3 and other uses throughout). The potential drop $\Delta\Phi_{\rm tip}$ is generally proportional to the tip field $E_{\rm tip}$, but has the advantage that it does not depend on the tip geometry. Nevertheless we will include $E_{\rm tip}$ estimates despite the much larger uncertainty because many other papers on leader and streamer propagation consider average electric fields over some distance rather than potential difference at a single point.

EXAMPLE: As an example of the model calculations, Figure 2 shows the leader potential and charge distribution for a negative leader with $r_C = 1$ m growing in a uniform ambient field $E_{amb} = 100$ kV/m, following the atmospheric electricity sign convention $E = \nabla\Phi$. The channel segment length is Δs=50 m. In this example the positive tip of the leader stays stationary, and the model values are plotted when the negative tip has reached distances of 500 m, 1000 m, 1500 m, and 2000 m. In Figure 2a the potential is uniform within the channel, but the value of Φ_{cha} increases as the negative leader tip extends through the uniform field. In a uniform field Φ_{cha} is equal to the potential at the middle of the channel. Beyond the ends of the leader the potential quickly returns to the ambient potential, as marked in black.

Figure 2b shows how the charge distribution changes as the leader propagates. In a uniform field the leader has equal amounts of positive and negative charge at the tips, tapering off to zero at the middle of the leader channel. As the leader propagates the symmetry of the charge distribution remains, but the magnitude of the charge at either end increases. Since only one tip is propagating in our example the zero charge point also moves. In a uniform field the zero charge point is always halfway along the leader. For an equipotential channel, the induced charge $\lambda(s)$ at each point is proportional to the difference between the channel potential Φ_{cha} and the ambient potential at that point

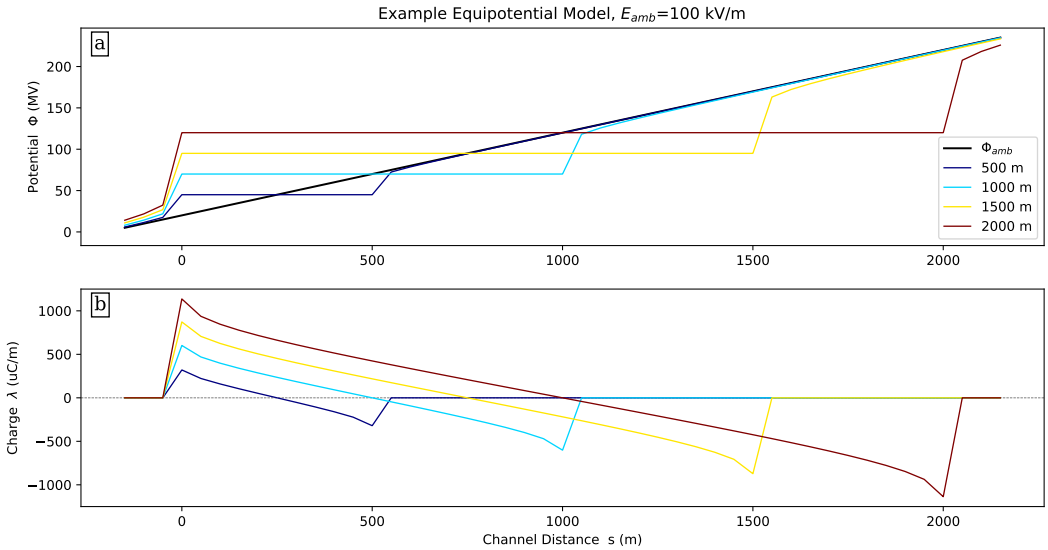

Figure 2. Examples calculations of the leader potential and charge distribution for various leader lengths in a uniform ambient field $E_{amb} = 100$ kV/m, following the atmospheric electricity sign convention $E = \nabla\Phi$. Plots show the potential along the leader channel (a), and the induced charge distribution (b).

$\Phi_{amb}(s)$, $\lambda(s) \propto \Phi_{cha} - \Phi_{amb}(s)$ as pointed out originally by Kasemir (1960). So the point on the leader with zero charge is the point where $\Phi_{cha} - \Phi_{amb}(s) = 0$, at the middle of the channel in this case. There is a slight enhancement to the charge density $\lambda(s)$ at the tips of the leader, beyond the value expected by a $\lambda(s) \propto \Phi_{cha} - \Phi_{amb}(s)$ relation (Figure 2b, the change in slope near the tips). This charge enhancement at the tips is related to the change in capacitance per unit length at the tips of a cylinder (Jackson, 2000).

3.2 Leader Tip Electric Field

Having estimated the ambient field and associated charge density along the channel, we also wish to estimate the electric field at the leader tip. Each segment of the leader is a uniformly charged cylinder of length Δs, radius r_C, with a linear charge density λ_i. The electric field along the s-axis from each cylindrical segment is given by

$$E_i(s) = \frac{\lambda_i}{2\pi r_C^2 \varepsilon_0}\left[\sqrt{r_C^2 + s^2} + \Delta s - \sqrt{r_C^2 + (\Delta s + s)^2}\right] \tag{8}$$

where in this case $s = 0$ is defined as the propagating end of the cylinder, and the equation is only valid ahead of the cylinder in the direction of propagation ($s \geq 0$). A derivation of Equation 8 is provided in Appendix A.

Equation 8 demonstrates that the field for each segment drops off very quickly over distances on the order of r_C. Thus, the field at the tip of the leader can be approximated as due to just the final segment. This field is highest right at the edge of the cylinder, so for $s = 0$

$$E_{\text{tip}}(0) = \frac{\lambda_{tip}}{2\pi r_C^2 \varepsilon_0}\left[r_C + \Delta s - \sqrt{r_C^2 + (\Delta s)^2}\right] \tag{9}$$

If we approximate Equation 9 using $r_C^2 + (\Delta s)^2 \approx (\Delta s)^2$, we get

$$E_{\text{tip}}(0) \approx \frac{\lambda_{tip}}{2\pi\varepsilon_0}\frac{1}{r_C} \tag{10}$$

Without further knowledge, the effective capacitive radius r_C for a dart leader channel could plausibly be anywhere from 1 mm (estimated dart leader conductive radius (Rakov, 1998)) to 100 m (streamer zone length at 10 km altitude observed by Edens et al. (2014)). Thus this $1/r_C$ dependence appears to pose a significant challenge in extracting any useful information about the magnitude of the tip field.

However, the electric field at a single point in a highly non-uniform field is not really useful in any case. More relevant to a discussion about streamer or breakdown activity at the tip would be the average field at the tip over some distance d

$$\overline{E_{\text{tip}}}(d) = \frac{1}{d}\int_0^d \frac{\lambda_{tip}}{2\pi r_C^2\varepsilon_0}\left[\sqrt{r_C^2+s^2} + \Delta s - \sqrt{r_C^2+(\Delta s+s)^2}\right] ds \tag{11}$$

which evaluates to

$$\begin{aligned}
\overline{E_{\text{tip}}}(d) = &\frac{\lambda_{tip}}{4\pi\varepsilon_0 d}\left[\ln\left(\frac{\sqrt{r_C^2+d^2}+d}{r_C}\right)\right. && (A)\\
&+\ln\left(\sqrt{r_C^2+\Delta s^2}+\Delta s\right) && (B)\\
&-\ln\left(\sqrt{r_C^2+(\Delta s+d)^2}+\Delta s+d\right) && (C)\\
&-\frac{\Delta s+d}{r_C^2}\sqrt{r_C^2+(\Delta s+d)^2} && (D)\\
&+\frac{d}{r_C^2}\sqrt{r_C^2+d^2} && (E)\\
&+\frac{\Delta s}{r_C^2}\sqrt{r_C^2+\Delta s^2} && (F)\\
&\left.+\frac{2d\Delta s}{r_C^2}\right] && (G)
\end{aligned} \tag{12}$$

where we have labeled each term (A, B, C, etc.). This integral was evaluated using Wolfram Alpha (Wolfram Research Inc., 2024).

Assuming $\Delta s >> d > r_C$ then $(B)+(C) \approx 0$. Applying the binomial approximation for $\frac{r_C^2}{(\Delta s+d)^2} < 1$, $\frac{r_C^2}{d^2} < 1$, and $\frac{r_C^2}{(\Delta s)^2} < 1$ to terms (D), (E), and (F) respectively, yields $(D)+(E)+(F)+(G) \approx \frac{1}{4}$. So we are left with

$$\overline{E_{\text{tip}}}(d) \approx \frac{\lambda_{tip}}{4\pi\varepsilon_0 d}\left[\ln\left(\frac{\sqrt{r_C^2+d^2}+d}{r_C}\right)+\frac{1}{4}\right] \tag{13}$$

If we choose $d = 1$ m then the difference in tip fields between $r_C = 0.001$ m and $r_C = 1$ m is about a factor of 7. This is still rather large, but at least gives an estimate of the tip field within about an order of magnitude, even across 3 orders of magnitude in radius. We do not use this approximation in the actual model calculations of E_{tip}, but it is useful for demonstrating the logarithmic dependency on r_C.

Additionally, the channel radius r_C is the effective radius of the cover charge initially deposited by streamers at the leader tip, and any subsequent changes to the cover charge by later corona or streamers (Bazelyan & Raizer, 2000, chapter 2.4). The radius r_C should then approximately correspond to the radius at which the radial electric field is equal to the streamer stability field. Assuming the axial and radial fields are the same

order of magnitude, one should expect $\overline{E_{\text{tip}}}(r_C)$ to be close to the value of the streamer stability field. If this condition is met then we can be more confident that we have chosen r_C correctly and our calculated E_{tip} values are essentially correct. A more sophisticated model would allow r_C to vary so that the radial field was always equal to the streamer stability field for each segment (e.g. Cooray et al. (2009)), but for now a simpler model with fixed r_C is used.

We note that E_{tip} as discussed in this section is essentially the "vacuum solution" field as defined by Celestin and Pasko (2011), we are not accounting for streamers forming ahead of the conductive leader tip. Streamers ahead of the tip would reduce the field at the tip by spreading the potential drop $\Delta\Phi_{\text{tip}}$ over a larger distance. Under typical approximations this would result in a constant E_{tip} equal to the streamer stability field E_{st}, which extends for a distance $L = \Delta\Phi_{\text{tip}}/(2E_{st})$ (Bazelyan & Raizer, 2000, page 69).

For E_{tip} in this paper we will report the values calculated from Equation 12 over a distance of d=1 m.

3.3 Ambient Electric Field Estimation

For any ambient electric field distribution we can calculate the charge distribution along the channel with Equation 5. If we can map the channel path parameter s_i to 3D coordinates (x_i, y_i, z_i) in the sky we can then calculate the vertical electrostatic field at a point (X, Y, Z_{grnd}) on the ground (where Z_{grnd} is the altitude of the ground above sea level) due to the charge distribution λ_i as:

$$E_z(X, Y, Z_{grnd}) = \sum_{i=1}^{N} \frac{\lambda_i \Delta s}{2\pi\varepsilon_0} \frac{z_i - Z_{grnd}}{\left[(x_i - X)^2 + (y_i - Y)^2 + (z_i - Z)^2\right]^{3/2}} \tag{14}$$

where the ground is treated as an ideal infinite conducting plane. Since the lightning channel is far from our field measurement locations, each segment of the channel can be approximated as a point charge. This calculation can be done for each time step t_k corresponding to a leader extension by Δs, to give the vertical field on the ground as a function of time, $E_z(X, Y, Z_{grnd}, t_k)$.

Typically for a lightning flash the ambient electric field $E_{amb}(s)$ is not known, but the vertical electric field at the ground $E_z(t)$ can be measured with an electric field change antenna. The extent of the conducting channel at any point in time can also be inferred from 3D lightning interferometer data. An initial guess can then be made for the ambient field $E_{amb}(s)$. For a conductive channel with endpoints at $s_a(t_k)$ and $s_b(t_k)$, the charge distribution $\lambda_i(t_k)$ induced by the guess $E_{amb}(s)$ can be calculated from Equation 5. The corresponding field change at the ground $E_z(t_k)$ can be calculated from Equation 14. The goodness-of-fit between the measured and modeled field changes can then be evaluated as

$$\chi^2 = \sum_{t_k} \frac{\left(E_{mod}(t_k) - E_{obs}(t_k)\right)^2}{\sigma_k^2} \tag{15}$$

where $E_{mod}(t_k)$ and $E_{obs}(t_k)$ are the modeled and observed fields, respectively, at time t_k, and σ_k is the estimated uncertainty in the observed field.

We can then find the ambient electric field $E_{amb}(s)$ which minimizes the χ^2 value iteratively using a non-linear optimization technique such as the Levenberg-Marquardt algorithm (Levenberg, 1944; Marquardt, 1963). The field on the ground does not depend strongly on each individual point $E_{amb}(s_i)$, so in order to limit the number of degrees of freedom we assume $E_{amb}(s)$ takes the form of a polynomial of order n, rather than

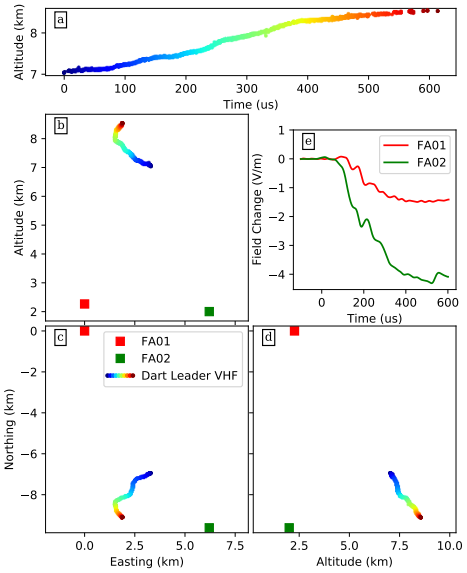

Figure 3. A plot of the path of the IC dart leader labeled K-5 over time relative to the two fast antennas. Panels are: altitude vs time (a), altitude vs easting (b), northing vs easting (c), and northing vs altitude (d). The points of K-5 are colored by time. The measured field change vs time at each station is also included (e), and the locations of the two fast antennas are marked in panels b, c, and d. The location of K-5 relative to the surrounding flash structure can be seen in Figure 3 of Jensen et al. (2023b).

individually fitting each value of $E_{amb}(s_i)$. Figure S1 in the supporting information shows the extreme case of polynomial order $n = 50$ in order to illustrate the results when allowing a large number of degrees of freedom. We also include a penalty in the χ^2 value for solutions where E_{tip} changes signs, since a real leader should stop propagating if this condition ever occurred. This penalty is chosen to be large enough to suppress sign changes in E_{tip}, but small enough that it does not upset the convergence of the solution or lead to significantly increased errors in Equation 15.

3.4 Model Implementation

Dart leader K-5 from Jensen et al. (2023b) was chosen to implement the model since this is a relatively simple IC dart leader. Figure 3 shows the known information for K-5, including the full 3D extent of the leader channel over time relative to the two fast antennas (FA01 and FA02), along with the electric field change vs time at the ground at these locations. This is the known information from which we want to estimate the unknown ambient electric field along the channel.

The leader path is simplified by smoothing the measured VHF source locations with a rolling average of the location over ± 20 μs. Equally spaced and consecutive points $\Delta s = 50$ m apart are selected to serve as the discrete leader segments in the model. The model includes a fixed channel radius of $r_C = 1$ m to account for charge being transported radially outward from the thin ($\sim$1 mm, (Rakov, 1998)) conducting core into the corona sheath/cover charge. To first order the capacitance of a long thin cylinder of length L and radius r_C is given by (Jackson, 2000):

$$C = \frac{2\pi\varepsilon_0 L}{\ln(L/r_C)} \tag{16}$$

The dependence of the estimated background field on the channel radius is thus weak, changing the modeled radius from 1 mm to 1 m only increases the capacitance by a factor of 2 for a L=1 km channel. The validity of the $r_C = 1$ m assumption in terms of the effect on the estimated tip electric field will be evaluated at the end of Section 4.1.

The channel of K-5 is obviously not perfectly straight. Since the axial field produced by each cylindrical segment (Equation 8) drops off quickly over distances on the order of $r_C << \Delta s$, only the nearest segments should contribute significantly to the potential at each point along the leader channel. Thus we assume that Equation 1 is still valid for the potential along a real tortuous leader channel as long the channel is approximately straight over distances of a few times Δs.

The field contributions from the channel segments and their image charges in the ground plane of the earth both fall off as approximately $1/R^2$, but the nearest channel segments are 25 m away, while most of the dart leaders in our flash occur about 5 km above the ground, placing the images charges 10 km below. The field contribution of the nearest channel segments is thus approximately $(10^4)^2/25^2 \sim 10^5$ times stronger than the contribution of the closest image charge, and we can safely ignore the image charges for leaders far from the ground.

We also assume that the dart leader channel starts with a conductive length of 100 m at t=0 in order to have some initial tip field and field change. Rather than skipping the first 100 m of dart leader development, we use the 3D map of the full flash to find a path along the same branch for 100 m in the direction opposite to the dart leader tip propagation. Negative values of channel distance s correspond to this "backward" direction along the branch. The negative dart leader tip starts at $s = 0$ at time $t = 0$.

4 Results

4.1 Estimated Cloud and Tip Fields

All electric fields in plots use the atmospheric electricity sign convention, i.e. for the ambient cloud E-field and tip E-field a positive E-field will accelerate electrons in the direction of leader propagation, $\hat{s}$. Since the behavior of the negatively charged dart leader tip is the subject of interest, this sign convention makes the plots easier to interpret.

Figure 4 shows the modeled field change (a and b) and estimated ambient field (c), where the ambient field is estimated using polynomials of various degrees n. The constant field ($n = 0$) is clearly a worse fit to the measured field changes than the higher polynomial degrees, which all result in similar field changes. All the modeled field changes seem to only fit the slow components of the measured field change, up to about 5 kHz. This is true even if we drastically increase the allowed degrees of freedom ($n = 50$ is shown in Figure S1 in the supporting information). This suggests that the higher frequency components of the field change (above ~5 kHz) are not associated with the general extension of the leader, but some other process which is not captured by our model. Since the higher frequency components do not seem to match between the two stations they may also be local interference at each station.

The $n > 0$ polynomial ambient fields (Figure 4c) generally decrease in the direction of dart leader extension as predicted in Jensen et al. (2023b) based on dart leader speed trends. Heckman (1992) also predicted electric fields which decrease along dart leader channels based on the way charge gets left behind as the channel decays, although this behavior has not been fully modeled. Since the $n = 3$ and $n = 4$ polynomials add extra oscillations and rapid changes in field strength without improving the fit to the fast antenna measurements (Figures 4a and 4b), we will specifically consider the n=2 case for the rest of our analysis. The same conclusions could be drawn from the $n = 1$ case since the ambient fields are similar.

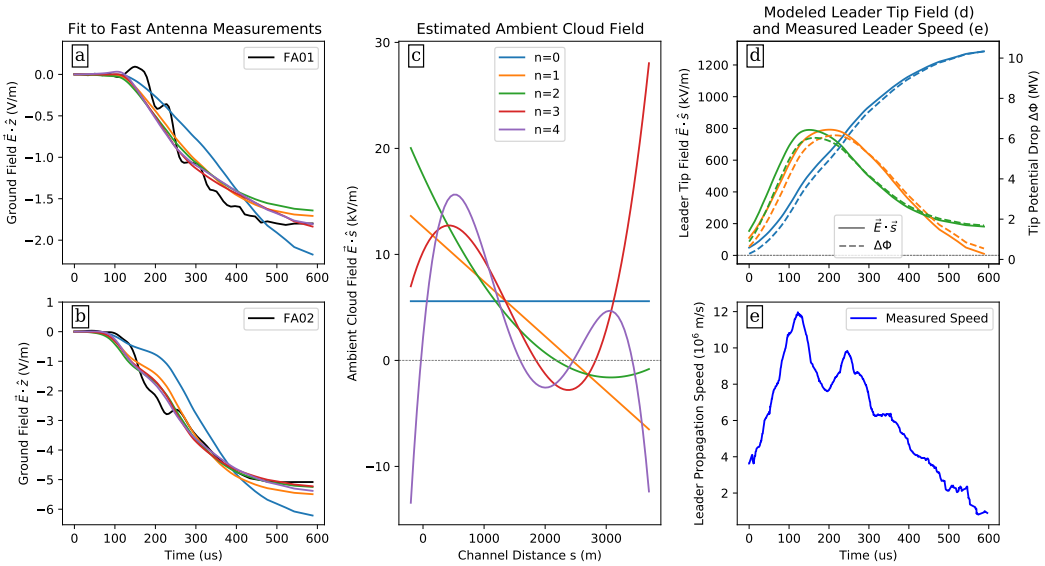

Figure 4. A plot of the modeled field change compared to the measured ground electric field change vs time (a and b), the estimated ambient cloud electric field vs channel distance (c), the estimated leader tip electric field E_{tip} vs time (d, left axis), and tip potential drop $\Delta\Phi_{\text{tip}}$ vs time (d, right axis), for various degrees n of polynomial ambient fields. We plot $|\Delta\Phi_{\text{tip}}|$ so the curves are not inverted compared to E_{tip}. The measured leader speed vs time (e) is included for comparison.

The ambient field values, which are mostly below 15 kV/m, are low compared to typical thunderstorm fields which are often measured to reach 50-100 kV/m (Marshall et al., 2001; Stolzenburg et al., 2007, 2015; Stolzenburg & Marshall, 2008). This is expected since the preceding leader, return stroke, and other discharge activities would have zeroed-out the field along the channel, and the ambient field estimated here therefore represents the recovery of the field along the channel as charge deposited in the corona sheath continues to diffuse radially outward between strokes. The estimated ambient field is thus only the ambient field at the location of the dart leader channel, for the duration of dart leader propagation. We cannot directly infer the ambient field at any other location or time.

The sign-change of the field in Figure 4c ($E_{amb} < 0$) is somewhat surprising, but the charge re-distribution during a lightning flash is complex, and it is possible dart leaders from other branches transported excess negative charge onto this branch while this branch was otherwise decayed and non-conducting.

Figure 4d shows the modeled leader tip field E_{tip} (solid, left axis) and tip potential drop $\Delta\Phi_{\text{tip}}$ (dashed, right axis) vs time. The $n = 3$ and $n = 4$ cases were omitted to make the plot less cluttered. The curves for E_{tip} and $\Delta\Phi_{\text{tip}}$ for a particular n value are nearly identical up to a scaling factor. In Figure 4d $|\Delta\Phi_{\text{tip}}|$ is plotted instead of $\Delta\Phi_{\text{tip}}$ for comparison with E_{tip} and easier interpretation. The $n = 1$ and $n = 2$ cases have an initial increase and gradual decreases of the tip field and potential drop, which is well correlated with the measured speed vs time of K-5 (Figure 4e), supporting our claim in Jensen et al. (2023b) that the leader speed is generally proportional to the leader tip field. With the current polynomial field approach, the model is incapable of catching small details such as the speed dip at 200 μs.

We include the $n = 0$ case in Figure 4d to demonstrate that in a uniform field the leader tip field and potential drop will increase indefinitely. The change in tip field with a change in length $\frac{d}{ds}[E_{\text{tip}}]$ is actually constant in a uniform field, but the slope $\frac{d}{dt}[E_{\text{tip}}]$ of the $n = 0$ curve is not constant in Figure 4d because we are using a non-constant leader speed ($\frac{d}{dt}[E_{\text{tip}}] = \frac{d}{ds}[E_{\text{tip}}]\frac{ds}{dt}$).

We may wish to compare our modeled tip fields to various field thresholds for traditional breakdown or streamer propagation. Gas discharge electric field thresholds are traditionally defined at sea level and room temperature, and they scale with air number density (N_{air}) (da Silva et al., 2019). The relative density compared to sea level and room temperature is $\delta = N_{\text{air}}(h, T)/N_{\text{air}}(h = 0 \text{ km}, T = 300 \text{ K})$, which can be approximated as

$$\delta(h, T) \approx \frac{300}{T} e^{-h/10.4} \tag{17}$$

where h is the height above sea level in kilometers and T is the temperature in Kelvin. The exponential term is a standard atmospheric approximation (Andrews, 2010, page 23), though Andrews calculates the density scale height assuming an isothermal atmosphere, and we include the temperature lapse rate as

$$H_0 = \frac{1}{\frac{gM}{RT_0} - \frac{L}{T_0}} \approx 10.4 \text{ km} \tag{18}$$

where $g = 9.8$ m/s^2 is the gravitational acceleration at earth's surface, $M = 0.029$ kg/mol is the molar mass of dry air, $R = 8.314$ J/(mol K) is the universal gas constant, $T_0 = 288.15$ K is the sea level standard temperature, and $L = 0.0065$ K/m is the temperature lapse rate (using relevant standard atmosphere values from Champion et al. (1985)). The temperature term in Equation 17 is derived from the ideal gas law, which can be rewritten as $N_{\text{air}} = p/k_B T$, where p is the pressure and k_B is Boltzmann's constant. So at equal pressures the gas number density is inversely proportional to the temperature.

Applying the altitude density scaling, at the altitude of ∼7 km above sea level, the breakdown field is expected to be $E_{\text{k0}} \cdot \delta \approx 1500$ kV/m, where $E_{\text{k0}} = 3000$ kV/m at sea level. From Figure 4d we see that the modeled tip fields are much lower than the breakdown threshold, especially at the beginning of propagation. This is surprising since this threshold should be the tip field required for leader propagation. However, since dart leaders propagate through pre-conditioned channels, the temperature may still be high from the previous lightning processes. If we assume a pre-dart-leader temperature of T=3000 K (Uman & Voshall, 1968), we get $E_{\text{k0}} \cdot \delta \approx 150$ kV/m, which is close to the modeled leader tip fields at the start of propagation (Figure 4d). Thus a dart leader could only propagate with the modeled initial tip field in a channel with $T \geq$3000 K, and a relatively high pre-dart-leader channel temperature (∼3000 K) may be required for dart leaders to initiate. The fact that the tip field never reaches the breakdown field for ambient air at 7 km may also explain why dart leaders typically do not form new branches and instead follow the existing flash structure. The range of tip field values we found are generally in agreement with the range of tip fields measured with Pockels sensors by Miki et al. (2002) in triggered lightning strikes, although their measurements were made near sea level. The tip potential drop estimates in Figure 4d are also in reasonable agreement with the "typical value" of 15 MV given for dart leaders in Rakov and Uman (2003) Table 1.1.

The fact that the estimated leader tip field is initially lower than even the nominal streamer stability fields in virgin air ($E_{\text{st0}-} \cdot \delta = 500-750$ kV/m at 7 km, (Babaeva & Naidis, 1997; Briels et al., 2008; Qin & Pasko, 2014)) may also explain the observation that the width of dart leader channels resolved in VHF is much narrower than those of stepped leaders (Hare et al., 2023a; Jensen et al., 2021; Shao et al., 2023). The fact that negative leaders are detected much more readily than positive leaders in VHF suggests that the observed VHF predominantly comes from negative streamers. The axial

field at the leader tip (E_{tip}) should also be the highest electric field at any point on the leader. So if E_{tip} is below the negative streamer stability threshold in virgin air there should be no negative streamers anywhere on the leader, except within the "warm" ($\sim$1000 K) pre-conditioned channel core with a radius on the order of centimeters (Uman & Voshall, 1968), where the air density is lower. Recalling that E_{tip} is the average field over 1 m, if E_{tip} is approximately equal to the virgin air stability field, and if the radial electric field near the tip is approximately equal to E_{tip}, then we may expect streamers out to a radius of about 1 m. This is in contrast to negative stepped leaders where E_{tip} is expected to be close to the breakdown field, and the streamer zone may have a radius of 10-100 m (Edens et al., 2014; Petersen & Beasley, 2013; Sonnenfeld et al., 2023).

In fact, our streamer zone estimates agree very well with the high speed video observations of Petersen and Beasley (2013). While they observed a radial streamer/corona zone of 10-20 m on a descending negative stepped leader, a later dart leader in the same channel had no visible radial streamer zone, although there is some faint uniform luminosity which may be corona. Instead of a wide radial streamer zone the dart leader exhibited a long forward streamer zone confined to the pre-conditioned channel, extending $\sim$20-40 m ahead of the leader tip. This long forward streamer zone is expected. If the air density in the pre-conditioned channel is $\sim$1/10th the ambient density, then the forward streamer zone within the pre-conditioned channel should be about 10 times longer than the radial streamer zone.

As discussed in Section 3.2 there is a large uncertainty in the modeled tip field values due to the uncertainty in the effective channel radius r_C. As also discussed in Section 3.2, however, r_C should be approximately the radius of the streamer zone that originally created the cover charge at the leader tip. The average electric field over a distance r_C ahead of the leader tip should thus be approximately equal to the streamer stability field ($\overline{E_{\text{tip}}}(r_C) \approx E_{\text{st0}-}$). Since we have defined E_{tip} to be the average electric field over 1 m, and the modeled E_{tip} values in Figure 4d are somewhat close to $E_{\text{st0}-} \cdot \delta \approx$ 500$-$750 kV/m on average, our choice of $r_C = 1$ m appears to be reasonable, certainly within an order of magnitude.

As a further comparison, from Figure 4d we can see that the average $\Delta\Phi_{\text{tip}}$ is about 4 MV. Using the streamer zone length approximation $L = \Delta\Phi_{\text{tip}}/(2E_{st})$ (Bazelyan & Raizer, 2000, page 69), we get $L = 2.7 - 4$ m (for $E_{\text{st0}-} \cdot \delta = 500 - 750$ kV/m). Again this is at least within an order of magnitude of our guess $r_C = 1$ m. We note that for a given ambient field in the cloud $\Delta\Phi_{\text{tip}}$ is completely independent of the leader tip geometry, so $r_C \approx \Delta\Phi_{\text{tip}}/(2E_{st})$ is a more straightforward estimate compared to using E_{tip}.

4.2 Speed, Tip Field, and Tip Current

Figure 5 shows a direct comparison between the measured leader speed, the modeled tip field, and square root of the modeled tip current vs time for the $n = 2$ case (Figure 4). In the Figure we have normalized each variable to a maximum value of 1 to remove any constants of proportionality. It is clear that the speed and tip fields are closely correlated, except for the speed dip at 200 μs and a small variation at the end. We do note that the correlation is not as strong for other orders n of the polynomial ambient field, and the correlation is also somewhat sensitive to how the errors are weighted in Equation 15 and model parameters. In fact, due to the ill-posed nature of the inverse problem there are essentially infinitely many ambient fields which could reproduce the measured field changes. Among these infinite solutions there are many possible ambient fields which result in E_{tip} curves that do not match the leader speed, although many are physically unreasonable. While we cannot therefore definitively conclude that the leader speed is proportional to the tip field as guessed in Jensen et al. (2021, 2023b), we

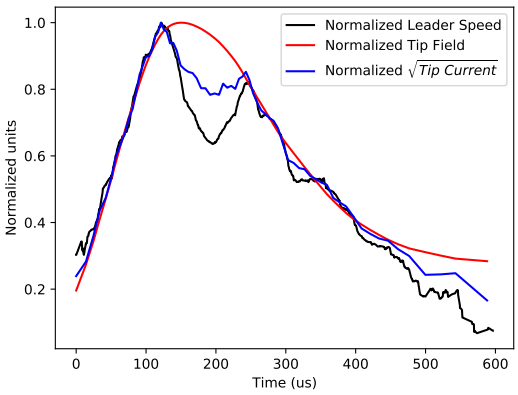

Figure 5. A plot of the normalized values of speed, tip field, and the square root of current vs time, for the $n = 2$ fit.

can at least claim that the observed field changes are consistent with a relationship of $v \propto E_{\text{tip}}$ for an equipotential leader.

If we frame the speed/field relationship as the leader mobility, $v = \mu E$, then we get a value of $\mu = 20$ m^2/Vs for this particular dart leader. As shown in Figure 4d the curves for E_{tip} and $\Delta\Phi_{\text{tip}}$ are essentially identical up to a scaling factor, so the dependence of the speed can be expressed in terms of either the tip field or potential drop. If we model the tip speed as $v = \eta\Delta\Phi_{\text{tip}}$ we get a value of about $\eta = 2$ m/Vs.

Since there is a fair amount of uncertainty in the correlation between tip field and speed we cannot completely rule out other power law relations such as the $v = a\Delta\Phi_{\text{tip}}^{1/2}$ relation suggested by Bazelyan and Raizer (2000) Equation 4.2. We note that the value of $a = 15$ m/(sV$^{1/2}$) suggested by Bazelyan and Raizer (2000) gives a speed 2 orders of magnitude too low even if we assume the relationship can be adjusted as $v = a\sqrt{\frac{\Phi_{\text{tip}}}{\delta}}$ for a 3000 K pre-dart-leader channel at 7 km altitude, where δ is defined in Equation 17. Regardless of the form of the relation, our results do suggest that the tip electric field or potential drop appears to be one of the main factors for the dart leader speed.

The square root of the tip current is also very well correlated with the speed in Figure 5, but this should not be surprising. If we re-write Equation 6 we can see that

$$I_{tip}(t_k) = -\Delta s \frac{\lambda_{tip}(t_k) - \lambda_{tip}(t_{k-1})}{t_k - t_{k-1}} = -\frac{\Delta s}{\Delta t}\lambda_{tip}(t_k) \tag{19}$$

where $\Delta s/\Delta t$ is just the speed of the leader, and we are making use of the fact that $\lambda_j(t_{k-1}) = 0$ for the advancing leader tip. This would suggest that $I_{tip} \propto v$, but we must further consider that from Equation 12 $\lambda_{tip} \propto E_{\text{tip}}$, so we must have $I_{tip} \propto vE_{\text{tip}}$. We have also just established that $v \propto E_{\text{tip}}$, so therefore $I_{tip} \propto v^2 \propto E^2$ is exactly the form we should expect. This result also generally agrees with numerical modeling of the streamer to leader transition by da Silva and Pasko (2013), and empirical relations suggested by Andreev et al. (2008) and Bazelyan and Raizer (1997)(page 213) based on laboratory spark experiments.

4.3 Other Model Results

Figure 6 shows the modeled potential, charge density, and current distributions along the leader colored by time, again for the $n = 2$ model. Each curve in Figure 6 is a snapshot of conditions along the entire plotted distance at a particular time indicated by the

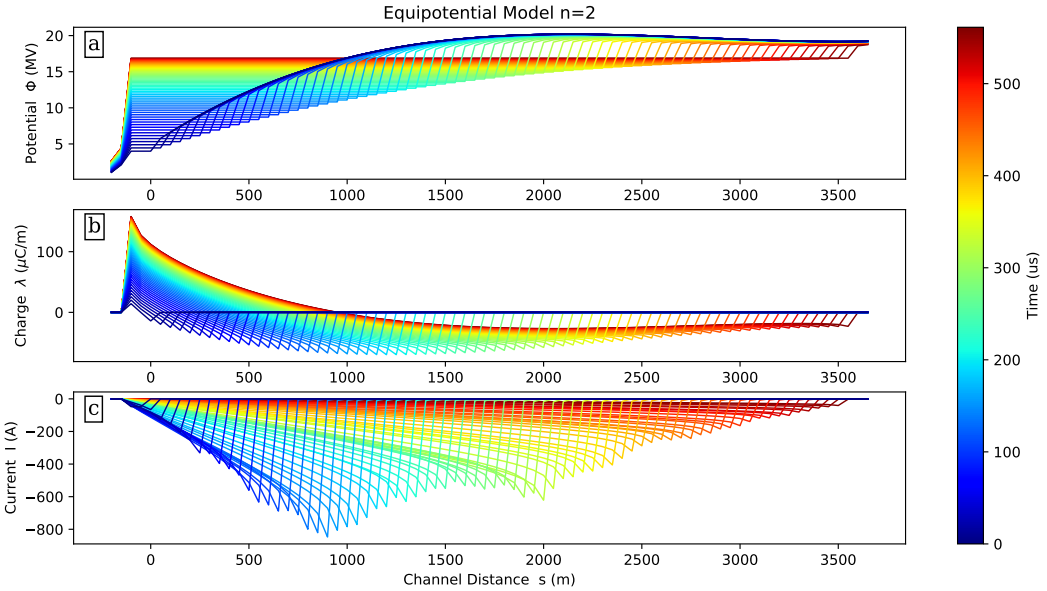

Figure 6. Plot of the potential distribution (a), charge density distribution (b), and current distribution (c) along the leader channel, colored by time, for the $n = 2$ polynomial ambient field. In all three plots the sharp increase at the leading edge indicates the leader tip position at that time.

color. Ahead of the negative leader tip at any point in time the charge and current are zero, and the potential quickly returns to the ambient potential as the leader tip field falls off as approximately $1/R^2$. The ambient potential for most of the channel ($s > 50$ m) can be seen as the darkest blue curve. The position of the propagating negative leader tip at each time step (each colored curve) is indicated by the sharp increase in the respective curves in all three panels of Figure 6. We also remind the reader that as a fundamental model assumption the potential is uniform within the channel, so the channel extent is indicated by horizontal lines in Figure 6a. Some distance past the positive tip of the leader (in the $-s$ direction) is also included to show the return to ambient conditions on that end.

Figure 6a shows that the potential along the active part of the channel is always a horizontal line due to the equipotential assumption, and the overall channel potential is increasing over time as the leader grows in length. If we consider the dart leader as transporting negative charge while leaving relatively stationary positive charge behind, then this increase in channel potential over time corresponds to an overall decrease in potential energy, as expected. We can also see that the charge distribution (Figure 6) essentially satisfies $\lambda(s) \propto \Phi_{cha} - \Phi_{amb}(s)$ away from the tips.

The amount of charge at the negative leader tip in Figure 6b does increase initially as in our simple dipole model in Jensen et al. (2023b), but then the charge at the tip decreases somewhat as the leader progresses. However, there is a larger deposit of charge behind the tip (negative charge from s=1000-3500) which remains present to the end of leader propagation. The charge density at the positive tip also increases continually as the leader progresses, although the increase is fastest at the beginning. The combined effects of the increasing positive tip charge, decreasing negative tip charge, and remaining negative charge along much of the channel may be the cause of the nearly constant tip charge in our previous dipole model as the leader slowed to a stop (Jensen et al., 2023b). The scale of the charge density at tens of μC/m is much smaller than typical charge den-

sity estimates of about 1 mC/m, but these estimates are typically for stepped leaders in virgin air, where the ambient fields (and thus charge density) are much higher.

The current in Figure 6c is highest right at the negative tip. For a more realistic channel with some finite conductivity we would expect this peak to follow a little behind the leader tip as the charge density at the tip takes some finite time to build.An example of this lagging current peak is presented by da Silva and Pasko (2015) (their Figure 5c). The amount the current peak lags behind the propagating tip depends on how fast the leader propagates relative to the timescale at which the new leader segment approaches equipotential with the rest of the channel. The current then drops off towards the stationary positive tip of the leader since the potential is not changing as much at that end. The peak current magnitude is about 800 A, which is in reasonable agreement with the "typical" dart leader current of 1 kA given in Rakov and Uman (2003) Table 1.1.

5 Discussion

5.1 Validity of the Equipotential Assumption

Our modelling results assume a perfect equipotential channel, therefore the conclusions we draw about dart leader propagation are only valid if real dart leader channels are approximately equipotential. In this section we put forward three arguments that dart leader channels are approximately equipotential, and that our modeling results are therefore valid.

First, a channel with finite conductivity σ_R will approach an equipotential over time, so the key question is how the time scale at which the channel reaches equipotential compares to the timescale of the leader propagation.

For a channel of length L, with conductivity σ_R, and conductive/resistive radius r_R, the total channel resistance is given by

$$R = \frac{L}{\sigma_R \pi r_R^2} \tag{20}$$

We can then estimate the timescale at which the leader approaches equipotential as $\tau \approx RC/10$ (see Appendix B for a derivation). Writing the equation out fully combining Equations 16 and 20 we have

$$\tau \approx \frac{1}{10} \frac{2\pi\varepsilon_0 L}{\ln(L/r_C)} \frac{L}{\sigma_R \pi r_R^2} \tag{21}$$

This time constant is derived assuming a channel of fixed length L suddenly becomes conductive in a uniform field, which does not really match the conditions of an extending channel in a non-uniform field, but it is still useful to consider the results of this simple approximation.

High speed spectroscopy observations of dart leaders suggest that they reach temperatures of ∼20 kK (Chang et al., 2017; Orville, 1975), which corresponds to equilibrium conductivity σ_R of about 10 kS/m (Chang et al., 2017; Yos, 1963). The conductive radius r_R of a dart leader channel is estimated to be about 1-4 mm (Rakov, 1998), and for a well developed dart leader it is likely to be closer to 4 mm. The channel for leader K-5 is about 3500 m long by the end of its propagation, so with r_R=4 mm and σ_R = 10 kS/m we get a time constant of τ=10 μs. Since 10 μs is short compared to the propagation timescale of dart leaders (100-1000 μs), the dart leader channel should be close to equipotential.

As a second argument, τ is also an estimate of how long it should take the field change to stop after propagation ceases. Any significant current in the channel will lead to a changing field at the ground. Ohm's Law $j = \sigma E$ suggests that the current will only drop

if either the field or conductivity drop. The channel conductivity is kept high by current heating the channel, so we should not expect the conductivity to drop while there is still significant current on the channel. Thus for a hot plasma channel the current will only stop when the field along the channel drops to essentially zero. Therefore the channel must be close to an equipotential when the field on the ground has stopped changing, and τ must also be low enough to allow the channel to reach equipotential by this time. Since the measured fields in Figures 4a and b have essentially stopped changing even before the leader has stopped propagating, we can assume that the leader is in fact close to an equipotential.

Finally, we consider the non-linear resistance of a plasma channel. A plasma channel with some applied current will quickly reach equilibrium between ohmic heating and heat losses. Laboratory experiments performed by Montano et al. (2006) suggest this happens on a time-scale around 1-10 μs. The associated resistance will cause the current in the channel to be somewhat less than the ideal equipotential current, and the channel will take longer to reach the equipotential charge distribution. Therefore there will be some remaining potential gradient along the channel $\nabla\Phi_{cha}$.

Laboratory experiments of free burning arcs suggest that for currents of about 100 A to 1000 A the steady state potential gradient is between 1 kV/m (King, 1962; Mazur & Ruhnke, 2014) and 2.5 kV/m (Montano et al., 2006). These potential gradients are small enough that they should not significantly change our results. To verify this we model dart leader K-5 while including such a potential gradient. We set the channel potential gradient $\nabla\Phi_{cha}$ to be equal to the constant gradient $\nabla\Phi_{const}$ as long as the resulting $\Phi_{cha}(s)$ is between $\Phi_{amb}(s)$ and the ideal equipotential value at each point. Otherwise, the channel remains at $\Phi_{cha}(s) = \Phi_{amb}(s)$. In keeping with our second argument for the equipotential model, we allow $\nabla\Phi_{cha}$ to approach zero as the leader slows to a stop. Based on Figure 11 of Montano et al. (2006), we drop $\nabla\Phi_{cha}$ to zero linearly over about 350 μs. Figures in the format of Figures 4 and 6 are included in the supporting information for $\nabla\Phi_{const}$=2.5 kV/m (Figures S2 and S3). We show the $n = 1$ ambient field because the $n = 2$ case has convergence issues when including the potential gradient. The results shown in those plots are very similar to the ideal equipotential results. Therefore, the results of our equipotential modeling are a good approximation of the true leader properties even if a real leader has some internal potential gradient. This is true as soon as the channel has reached equilibrium between ohmic heating and heat losses, which occurs within 1-10 μs (Montano et al., 2006).

5.2 Branch Junctions

In Jensen et al. (2023b), we hypothesized that the rapid speed variations as dart leaders passed branch junctions may be caused by charge deposits near those junctions. If the two branches were previously conductive at different times, they may be at very different potentials, and a significant amount of charge would be deposited at the transition from one potential to the other. The negative dart leader tip would be repelled by a negative charge deposit near the junction, so that the dart leader might decelerate while approaching the junction and accelerate after passing it.

It is clear from the results in Section 4 that rapid variations in the ambient field are not resolved based purely on fitting to the measured field changes at the ground. In order to test our branch junction hypothesis explicitly, we need to modify our approach. Since the results in Section 4.2 do suggest a correlation between the tip field E_{tip} and the leader speed, we add this as another constraint using our assumed relationship of $v = \mu E_{\text{tip}}$, leading to a χ^2 value

$$\chi^2_{speed} = \sum_{t_k} \frac{\left(\mu E_{\text{tip}}(t_k) - v_{obs}(t_k)\right)^2}{\sigma^2_{speed}} \tag{22}$$

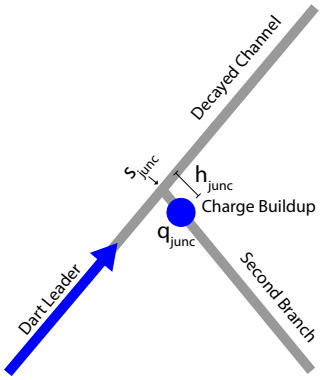

Figure 7. A diagram showing the configuration of the branch junction charge as hypothesized in Jensen et al. (2023b) The junction between branches is located at a point s_{junc}. A charge q_{junc} is located a perpendicular distance h_{junc} away from the junction point, along the second branch.

We also add a term to the ambient field which corresponds to the charge configuration in Figure 7. For a branch junction at location s_{junc} with a point charge q_{junc} at a distance h_{junc} along the perpendicular second branch, the resulting electric field on the leader channel is

$$E_{junc}(s) = \frac{q_{junc}}{4\pi\varepsilon_0} \frac{s - s_{junc}}{\left[(s - s_{junc})^2 + h_{junc}^2\right]^{3/2}} \tag{23}$$

where we are treating the channel as perfectly straight for simplicity, and calculating the $\vec{E}_{junc} \cdot \hat{s}$ component of the field.

To avoid having the junction charge significantly modify the field fit away from the junction, we find the fitting parameters in two stages. First, h_{junc} and q_{junc} are fit using the Levenberg-Marquardt algorithm, while using an assumed value of s_{junc}=1675 m since this is where the change in speed is observed along the channel. The same $n = 2$ ambient field previously found in section 4 is used as the background field. The value of $\mu = 20$ m^2/(Vs) from Section 4.2 is also used so that the proportionality between the speed and tip field remains the same. The time range of Equation 22 is limited to $t = 100$ μs to $t = 260$ μs, since this is the range of the dip in the observed speed (Figure 4). This way we are fitting the dip specifically without trying to optimize the fit for other times. For the fast antenna field change fit we continue to use the full time range. The combined goodness of fit parameter is then $\chi^2_{\text{tot}} = \chi^2_{\text{FA01}} + \chi^2_{\text{FA02}} + \alpha\chi^2_{\text{speed}}$ where α is a weighting term which we adjusted manually to achieve a reasonable balance between fitting the field change and the speed.

After finding a reasonable fit for the junction point charge parameters, we then refit the background field with a 2nd order polynomial in order to find a better fit with both terms present. This process could be repeated iteratively, alternating between junction charge and background field fits, but we found one iteration was enough in this case. It may also be possible to fit the junction charge and background field both at the same time, but due to issue with convergence to the optimal result and the need for human judgement in weighting the χ^2 values, the two stage approach was more tractable.

The results from this process are shown in Figure 8. Figures 8a and 8b show essentially the same field change at the ground as the $n = 2$ results in Figures 4a and 4b. The ambient field in Figure 8 includes the 2nd order polynomial background field, the junction charge field from Equation 23, and the sum of the two field terms. The best fit

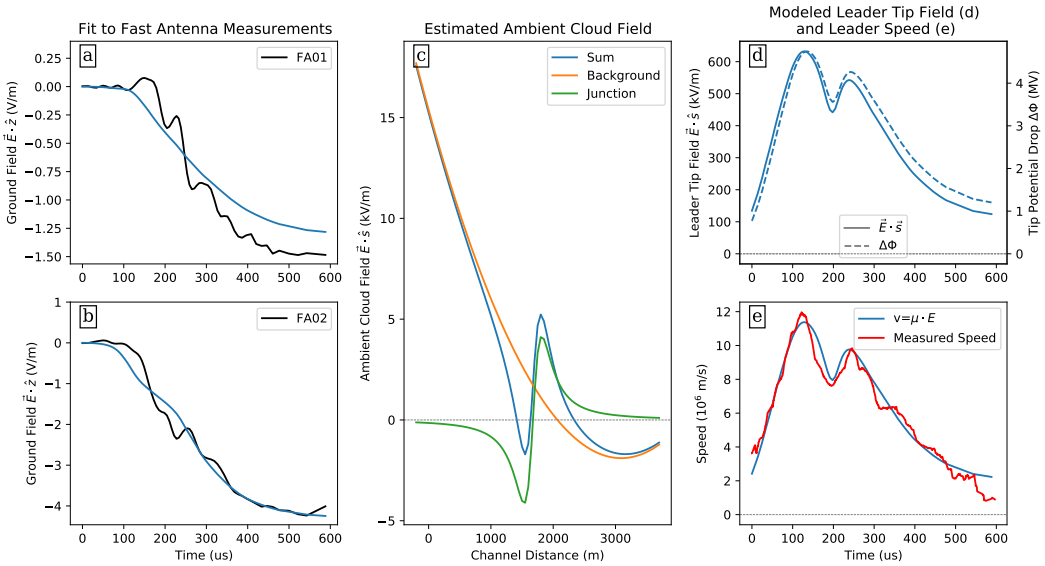

Figure 8. Equipotential model results when adding the junction charge term to the n=2 ambient field from Section 4. In the same format as Figure 4, the plot shows the measured and fit field change vs time for FA01 (a) and FA02 (b), the ambient field vs channel distance (c) including the background 2nd order polynomial field, the junction charge field, and the sum of these two components. The leader tip field vs time (d, left axis) and tip potential drop vs time (d, right axis) is shown, along with the measured and modeled leader speed vs time (e).

values are h_{junc}=332 m and q_{junc}=−115 mC. The tip field and tip potential drop vs time in Figure 8d show a pronounced dip around the location of the dip in speed in Figure 8e. We further include the modeled $v = \mu E$ in Figure 8e, in general there is now an excellent agreement with the measured leader speed for the whole leader duration.

We note that there is no branch visible in the BIMAP-3D sources at the s_{junc}=1675 m location of the simulated charge, even when we include all VHF sources from the full recorded flash. There are multiple small side branches within a few hundred meters of this location that appear in VHF either before or after K-5, and possibly the speed variation we observe is due to the combined influence of these multiple side branches. It is also possible that some previous leader activity deposited charge directly along the channel without the need for a branch junction. Ultimately, our modeling, in conjunction with the observation of speed variations, suggests the presence of some excess charge along the channel, although the source of this charge is not clear in this case. Either way, we have at least demonstrated that our hypothesis from Jensen et al. (2023b) is generally viable. We have reinforced our conclusion from Section 4.2 that, using the equipotential model, a leader speed relationship of $v = \mu E_{\text{tip}}$ is consistent with both our observations of field changes at the ground and the observed leader speed. Further, under the equipotential model it is possible for a charge deposit a relatively short distance from the primary channel to cause E_{tip} to exhibit a rapid drop and recovery, like the branch junction speed changes reported in Jensen et al. (2023b), without significantly changing the field change measured at the ground.

5.3 Bidirectional Development

High speed camera observations of dart leaders initiating outside of clouds indicate that the bright channel initially extends bidirectionally, but the extension in the pos-

itive tip direction quickly halts once it reaches the previously observed end of the pre-conditioned channel (Ding et al., 2024; Mazur, 2016). Unfortunately, this extension in the positive direction is not observed in VHF by BIMAP-3D.

We have performed some tests assuming the positive tip extends at the same speed as the negative tip until it reaches the end of the branch as observed in earlier VHF. Plots showing the K-5 results when including this bidirectional development are included in the supporting information (Figures S4 and S5), in the style of Figures 4 and 6. The estimated ambient field is somewhat lower in magnitude when including bidirectional development, but still generally decreases in the direction of propagation. The modeled negative tip field is slightly lower, peaking at about 500 kV/m rather than 800 kV/m, but it is still generally correlated with the leader speed. Thus the inclusion of this bidirectional development does not significantly change any of our conclusions. The most significant change is that the current is high at both leader tips while they are propagating, with a more uniform current through the middle of the channel. After the positive tip reaches the inferred end of the branch and stops propagating, the current distribution is similar to the distribution shown in Figure 6.

Figure S4d in the supporting information also includes the tip field and potential drop for the positive tip of the dart leader. The positive tip field is below the the ambient air breakdown field. This model result is consistent with the optical observation that the fast bidirectional development stops once it reaches the end of the pre-conditioned channel (Ding et al., 2024; Mazur, 2016). As reported by Jensen et al. (2023b), the positive tip appears to continue extending at $2{\times}10^4$ m/s throughout the dart leader phase of the flash. Our new modeling results suggest this 2×10^4 m/s positive tip extension may occur with a tip field above the positive streamer stability threshold but below the breakdown field in virgin air.

5.4 Other Dart Leaders

We also estimated ambient fields and tip fields for several other IC dart leaders from the same flash analyzed in Jensen et al. (2023b). Figures for these are included in the supporting information (Figures S6 - S15) to avoid an excessive number of figures in the main text. The path each dart leader follows can be seen in the figures of Jensen et al. (2023b), or the figures and animations in the supplementary material for that paper (Jensen et al., 2023a).

In most cases shown in the supporting information we were able to find ambient fields such that the modeled leader fit both the measured field changes, while also having a tip field which was generally correlated with the leader speed. In all these valid cases the estimated cloud field generally decreases along the channel length, similar to Figure 4c. The highest field values are also similarly low, less than about 10-15 kV/m.

In general the modeled leader tip fields seem to explain the major trends in increasing or decreasing average leader speed, while failing to capture the more complex speed variations of some leaders. These generally support our conclusion that the observed leader speed trends can be explained as $v \propto E_{\text{tip}}$ for an equipotential leader, especially considering we are estimating the ambient field with only a few degrees of freedom, so we cannot expect to match complicated variations in speed.

For the empirical relation $v = \mu E_{\text{tip}}$ we find μ values ranging between 10-30 m^2/Vs. For the relation $v = \eta \Delta\Phi_{\text{tip}}$ we find η values ranging between 1-4 m/Vs. Since our uncertainties are large and the quality of fit varies for each leader we cannot say whether the differences in these values among different dart leaders are caused by random uncertainty, or if they reflect something more fundamental like the temperature of the pre-dart-leader channel in each case.

In a few cases (the full K-8 and K-13, Figures S11 and S15 respectively) we were not able to match the measured field changes from both stations. These cases indicate that it is possible for a dart leader to have a more complicated field change even if the observed development in VHF seems fairly simple. Comparing the field change timing (Figures S11 and S15) to the leader development (Jensen et al., 2023a), for both K-8 Full and K-13, the shift towards a positive field change at FA02 occurs close to the time that those dart leaders reach junction J1. This strongly indicates that the more complicated field changes are caused by VHF invisible development into the other branch at J1. These cases are included to show that while our equipotential model constrained by the BIMAP-3D observations works in most cases, there are some exceptions.

6 Summary and Conclusions

In this paper we have modeled dart leaders with a contemporary version of the equipotential leader model first proposed by Kasemir (1960). Using the observed 3D dart leader development and ground electric field changes, along with the equipotential model, we then applied standard inverse problem techniques to estimate the ambient field in the cloud. The equipotential model then also provided some insights into the development of the channel, including the channel potential, charge density, and current, along with the electric field at the leader tip. Due to the integral nature of the electrostatic field change at the ground in Equation 14, there are essentially an infinite number of ambient field solutions which will fit the observed field changes, even when constrained by the path and speed of leader development as observed by BIMAP-3D. Solving for this ambient field is thus an "ill-posed" inverse problem. The modeled dart leader channel properties are therefore not definitive, but are at least consistent with our observations. The fact that our modeled results seem to explain more general observed properties of dart leaders, and the fact that we obtained most of these model results using only simple linear or quadratic ambient fields lends further credibility to our claims.

The following conclusions, listed according to their corresponding section within this paper, are consistent with our observations:

Section 4.1

1. A physically plausible ambient field E_{amb} that matches VHF observations of channel development and electric field changes at the ground can be found.
2. The estimated ambient field along the dart leader channel is generally low, less than 15 kV/m ($0.01 E_{\mathrm{k0}} \delta$ at 7 km), and decreasing in the direction of dart leader propagation.
3. The modeled E_{tip} and $\Delta\Phi_{\mathrm{tip}}$ are essentially proportional to each other.
4. E_{tip} is generally less than the normal breakdown threshold at 7 km and ambient temperature. This possibly explains why dart leaders are typically confined to preconditioned channels.
5. The modeled E_{tip} values are close to the negative streamer stability field in ambient air $E_{\mathrm{st0-}} \cdot \delta$, suggesting that negative streamers should only extend a few meters radially outward from the channel, in agreement with VHF observations of narrow dart leader channels (Hare et al., 2023a; Jensen et al., 2021; Shao et al., 2023).

Section 4.2

6. E_{tip} and $\Delta\Phi_{\mathrm{tip}}$ are correlated with the observed leader propagation speed.
7. The square root of the current at the leader tip is also correlated with leader speed, this is expected since the model equations yield $I_{tip} \propto v \cdot E_{\mathrm{tip}}$ and our model results show $E_{\mathrm{tip}} \propto v$.

Section 4.3

8. The equipotential model allows calculation of the potential of the leader channel, as well as the charge and current distributions, all resolved in time and space.

Section 5.1

9. The equipotential model is a good approximation of the true leader properties.

Section 5.2

10. A charge deposit near the channel can produce tip field variations which could explain the speed variations we observed associated with branch junctions in Jensen et al. (2023b).

Section 5.4

11. Similar results to the above conclusions (1-10) can be obtained for several other dart leaders from the same flash.
12. For the empirical relation $v = \mu E_{\text{tip}}$ we find typical values of μ=10-30 m^2/Vs.
13. For the empirical relation $v = \eta \Delta\Phi_{\text{tip}}$ we find typical values of η=1-4 m/Vs.
14. In a few cases the model cannot fit the observed field changes at both stations simultaneously, we suggest these cases may correspond to VHF invisible development along other branches in the flash structure.

In addition to specific insights we have gained into dart leader development, we hope this paper ultimately serves as a proof-of-concept for a method to combine observations and physics-based modeling in order to improve our understanding of lightning processes in general.

Appendix A Cylinder Tip Field Derivation

The electric field produced by any uniform volume of charge is given by

$$\vec{E} = \frac{1}{4\pi\varepsilon_0} \iiint \frac{\rho}{R^3} \vec{R} dV \tag{A1}$$

Consider a uniformly charged cylinder, and the electric field produced along the $\hat{z}$ axis. By symmetry, the electric field will only be in the $\hat{z}$ direction, so we can replace $\vec{R}$ with $\vec{R} \cdot \hat{z} = z$. We will also have $R = \sqrt{r'^2 + z^2}$, and the volume element becomes $dV = r' d\phi dr' dz$. So we have

$$E_{cyl}(z) = \frac{1}{4\pi\varepsilon_0} \int\int\int_0^{2\pi} \frac{\rho z r'}{(r'^2 + z^2)^{3/2}} d\phi dr' dz = \frac{1}{2\varepsilon_0} \int\int \frac{\rho z r'}{(r'^2 + z^2)^{3/2}} dr' dz \tag{A2}$$

where the integral over ϕ is trivial since there is no ϕ dependence. The term in the integral should be recognizable as the electric field on the axis of a ring of uniform charge with radius r', for a total charge $\rho r'$ (with appropriate units for ρ).

If the cylinder of charge has radius r then the integral over r' is

$$E_{cyl}(z) = \frac{1}{2\varepsilon_0} \int\int_0^r \frac{\rho z r'}{(r'^2 + z^2)^{3/2}} dr' dz = \frac{1}{2\varepsilon_0} \int \left[-\frac{\rho z}{\sqrt{r'^2 + z^2}} \right]\Bigg|_0^r dz \tag{A3}$$

which evaluates to

$$E_{cyl}(z) = \frac{\rho}{2\varepsilon_0} \int \left(1 - \frac{z}{\sqrt{r^2 + z^2}} \right) dz \tag{A4}$$

where this equation without the integral should be recognizable as the electric field on the axis of a uniformly charged disk, where ρ would be a surface charge density instead of a volume density.

To find the field from the full cylinder we then integrate over uniformly charged disks at location z', so we substitute $z \to z - z'$, and integrate over z'. For a cylinder that extends from $z' = -L$ to $z' = 0$ the integral is then

$$E_{cyl}(z) = \frac{\rho}{2\varepsilon_0} \int_{-L}^{0} \left(1 - \frac{(z - z')}{\sqrt{r^2 + (z - z')^2}} \right) dz' = \frac{\rho}{2\varepsilon_0} \left[z' + \sqrt{r^2 + (z - z')^2} \right]\Bigg|_{-L}^{0} \tag{A5}$$

which evaluates to

$$E_{cyl}(z) = \frac{\rho}{2\varepsilon_0}\left[\sqrt{r^2+z^2} + L - \sqrt{r^2+(z+L)^2}\right] \tag{A6}$$

This is the same as Equation 8 in the main text if we substitute $z \to s$, $L \to \Delta s$, and $\rho \to \lambda/(2\pi r^2)$.

Appendix B Time Constant Derivation

To first order, the self-capacitance C_{tot} of a long cylindrical leader channel is given by Equation 16. The total resistance R_{tot} of the channel is then given by Equation 20. If we split this leader channel into N discrete segments then each segment has capacitance C_{tot}/N and resistance R_{tot}/N. We note that the capacitance C_{tot}/N is not between the channel and some hypothetical co-axial shell, but rather the self-capacitance between each cylindrical segment of length L/N and every other segment of the channel.

If the leader is initially non-conductive in a uniform electric field, and then suddenly becomes conductive, this is analogous to being driven by equal and opposite voltages at the two ends, and then having the voltage supplies suddenly disconnected. We set the potential at the center of the leader to 0 for convenience since the channel will approach the central potential in a uniform field (Equation 2).

First we consider the simple case of N=2 segments. We then have an electrical circuit with two capacitors of value $C = C_{tot}/2$, separated by a resistor of value $R = R_{tot}/2$, as shown in Figure B1a. If this circuit is driven by equal and opposite voltages $+V$ and $-V$ (analogous to a leader channel in a uniform field), then by symmetry the voltage must always be 0 in the middle of the resistor, and the circuit in Figure B1a is equivalent to the circuit in Figure B1b (up to the sign of the voltage). The circuit in Figure B1b is a regular RC circuit, so we can immediately see that the time constant is $\tau = (R_{tot}/4)(C_{tot}/2) = R_{tot}C_{tot}/8$. For N=2 our choice of $R = R_{tot}/2$ is somewhat contrived, but as N gets larger the difference between R_{tot} and $R_{tot}(N-1)/N$ becomes negligibly small.

We then consider the N=4 case, shown in Figure B1c. Again by symmetry we can see that the voltage at the center of the middle resistor must always be zero, and thus the discharging circuit is equivalent to Figure B1d. After applying Kirchoff's node law for this circuit and substituting the relevant terms in voltage and $\frac{dV}{dt}$ we get a system of ordinary differential equations

$$\frac{dV_1}{dt} = \frac{16}{R_{tot}C_{tot}}(-V_1 + V_2) \tag{B1}$$

$$\frac{dV_2}{dt} = \frac{16}{R_{tot}C_{tot}}(V_1 - 3V_2) \tag{B2}$$

where V_1 and V_2 are indicated in Figure B1d.

This system of differential equations can be re-framed as an eigenvalue problem by writing the system as

$$\frac{d}{dt}\begin{bmatrix}V_1\\V_2\end{bmatrix} = \frac{16}{R_{tot}C_{tot}}\begin{bmatrix}-1 & 1\\1 & -3\end{bmatrix}\begin{bmatrix}V_1\\V_2\end{bmatrix} \tag{B3}$$

which has a solution of the form

$$\vec{V} = \vec{X}e^{\lambda t} \tag{B4}$$

where $\vec{X}$ is an eigenvector and λ is the corresponding eigenvalue of the matrix in Equation B3. The system of capacitors will then have two time constants corresponding to the eigenvalues $\tau = 1/\lambda$. In this case the eigenvalues and corresponding eigenvectors are

$$\lambda = \frac{16}{R_{tot}C_{tot}}(\pm\sqrt{2} - 2); \quad \vec{X} = \begin{bmatrix}1 \pm \sqrt{2}\\1\end{bmatrix} \tag{B5}$$

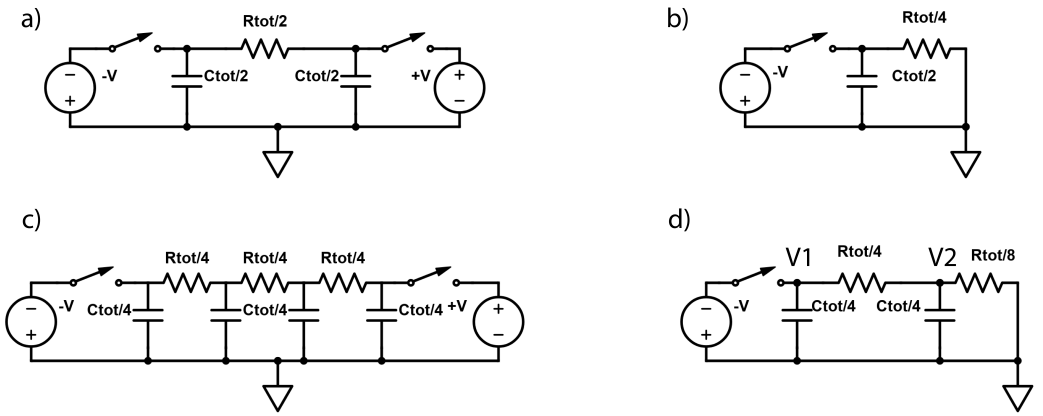

Figure B1. Circuit diagram showing the N=2 (a, b) and N=4 (c, d) simple model of a leader in a uniform field as N capacitors connected by N-1 resistors, with the capacitors driven by equal and opposite voltages across switches. On the right (b, d) we see the equivalent circuits reduced by symmetry.

The full solution will be a linear combination of solutions of the form given in Equation B4 for the two eigenvalue/eigenvector pairs, but for our purposes we are interested only in the time constants $\tau = 1/\lambda$. Since we are trying to estimate an upper bound for the timescale at which a leader channel reaches equipotential, we are interested in the long run behavior ($t \to \infty$). The faster time constant term will decay more quickly, leaving the slower time constant term to dominate in the long run. This time constant is

$$\tau = \frac{R_{tot}C_{tot}}{16(2-\sqrt{2})} \approx \frac{R_{tot}C_{tot}}{9.37} \tag{B6}$$

Checking higher orders of N with numerical simulations we find that the decay time remains within the range

$$\frac{R_{tot}C_{tot}}{8} < \tau < \frac{R_{tot}C_{tot}}{10} \tag{B7}$$

We thus suggest $\tau = RC/10$ as a convenient rule of thumb for the timescale at which a lightning channel becomes an equipotential. Strictly speaking this approximation is only valid for a stationary channel which suddenly develops in a uniform field, but it may still be a useful reference for a more realistic model of leader development.

Appendix C Open Research

The 3D mapping and field change data used for this paper has previously been made available online (Jensen et al., 2023a). All data files are in text format with headers that describe each data column. A PDF is included which describes the included files, and gives examples of the headers and column format.

Acknowledgments

We would like to acknowledge an undergraduate student paper written by Qianui Qi of the Pennsylvania State University: Department of Electrical Engineering for providing the initial framework for the equipotential model calculations, as an adapted form of the methods reported by Mazur and Ruhnke (1998). We would also like to thank Steve Cum-

mer for suggesting that we explicitly model the branch junction interaction when an early version of this work was presented at the AGU 2023 Fall Meeting.

Research presented in this article was supported by Los Alamos National Laboratory through the Laboratory Directed Research and Development program under project number 20230223ER, and the Center for Space and Environmental Science under project number YW0900. Additional funding for this work was provided by the New Mexico Consortium under #Subcontract No: 038508 to New Mexico Institute of Mining and Technology.

References

Andreev, A., Bazelyan, E., Bulatov, M., Kuzhekin, I., Makalsky, L., Sukharevskij, D., & Syssoev, V. (2008). Experimental study of the positive leader velocity as a function of the current in the initial and final-jump phases of a spark discharge. *Plasma Physics Reports*, *34*, 609–615. Retrieved from https://doi.org/10.1134/S1063780X0807009X

Andrews, D. G. (2010). *An introduction to atmospheric physics.* Cambridge University Press. Retrieved from https://dl.icdst.org/pdfs/files1/4a12b8f80ceb22105a190e71d78bed02.pdf

Babaeva, N., & Naidis, G. (1997). Dynamics of positive and negative streamers in air in weak uniform electric fields. *IEEE Transactions on Plasma Science*, *25*(2), 375-379. doi: 10.1109/27.602514

Bazelyan, E. M., & Raizer, Y. P. (1997). *Spark discharge.* CRC press.

Bazelyan, E. M., & Raizer, Y. P. (2000). *Lightning physics and lightning protection.* CRC Press.

Briels, T. M. P., Kos, J., Winands, G. J. J., van Veldhuizen, E. M., & Ebert, U. (2008, nov). Positive and negative streamers in ambient air: measuring diameter, velocity and dissipated energy. *Journal of Physics D: Applied Physics*, *41*(23), 234004. Retrieved from https://dx.doi.org/10.1088/0022-3727/41/23/234004 doi: 10.1088/0022-3727/41/23/234004

Cai, L., Chu, W., Wang, J., Zhou, M., Yan, Y., Tian, R., & Fan, Y. (2022). Observation and modeling of dart leader development in an altitude-triggered lightning flash. *Journal of Geophysical Research: Atmospheres*, *127*(24), e2022JD037545. Retrieved from https://agupubs.onlinelibrary.wiley.com/doi/abs/10.1029/2022JD037545 (e2022JD037545 2022JD037545) doi: https://doi.org/10.1029/2022JD037545

Celestin, S., & Pasko, V. P. (2011). Energy and fluxes of thermal runaway electrons produced by exponential growth of streamers during the stepping of lightning leaders and in transient luminous events. *Journal of Geophysical Research: Space Physics*, *116*(A3). Retrieved from https://agupubs.onlinelibrary.wiley.com/doi/abs/10.1029/2010JA016260 doi: https://doi.org/10.1029/2010JA016260

Champion, K., Cole, A., & Kantor, A. (1985). Standard and reference atmospheres. *Handbook of geophysics and the space environment*, *14*. Retrieved from https://citeseerx.ist.psu.edu/document?repid=rep1&type=pdf&doi=f8c836290a985f56e88725192391589c185f205d

Chang, X., Yuan, P., Cen, J., & Wang, X. (2017). Variation of the channel temperature in the transmission of lightning leader. *Journal of Atmospheric and Solar-Terrestrial Physics*, *159*, 41-47. Retrieved from https://www.sciencedirect.com/science/article/pii/S1364682617300123 doi: https://doi.org/10.1016/j.jastp.2017.04.006

Chen, M., Zheng, D., Du, Y., & Zhang, Y. (2013). Evolution of line charge density of steadily-developing upward positive leaders in triggered lightning. *Journal of Geophysical Research: Atmospheres*, *118*(10), 4670-4678. Retrieved from

https://agupubs.onlinelibrary.wiley.com/doi/abs/10.1002/jgrd.50446 doi: https://doi.org/10.1002/jgrd.50446

Cooray, V., Becerra, M., & Rakov, V. (2009). On the electric field at the tip of dart leaders in lightning flashes. *Journal of Atmospheric and Solar-Terrestrial Physics*, *71*(12), 1397-1404. Retrieved from https://www.sciencedirect.com/science/article/pii/S1364682609001497 doi: https://doi.org/10.1016/j.jastp.2009.06.002

Cummer, S. A. (2020). Indirectly measured ambient electric fields for lightning initiation in fast breakdown regions. *Geophysical Research Letters*, *47*(4), e2019GL086089. Retrieved from https://agupubs.onlinelibrary.wiley.com/doi/abs/10.1029/2019GL086089 (e2019GL086089 10.1029/2019GL086089) doi: https://doi.org/10.1029/2019GL086089

da Silva, C. L., & Pasko, V. P. (2013). Dynamics of streamer-to-leader transition at reduced air densities and its implications for propagation of lightning leaders and gigantic jets. *Journal of Geophysical Research: Atmospheres*, *118*(24), 13,561-13,590. Retrieved from https://agupubs.onlinelibrary.wiley.com/doi/abs/10.1002/2013JD020618 doi: https://doi.org/10.1002/2013JD020618

da Silva, C. L., & Pasko, V. P. (2015). Physical mechanism of initial breakdown pulses and narrow bipolar events in lightning discharges. *Journal of Geophysical Research: Atmospheres*, *120*(10), 4989-5009. Retrieved from https://agupubs.onlinelibrary.wiley.com/doi/abs/10.1002/2015JD023209 doi: https://doi.org/10.1002/2015JD023209

da Silva, C. L., Sonnenfeld, R. G., Edens, H. E., Krehbiel, P. R., Quick, M. G., & Koshak, W. J. (2019). The plasma nature of lightning channels and the resulting nonlinear resistance. *Journal of Geophysical Research: Atmospheres*, *124*(16), 9442-9463. Retrieved from https://agupubs.onlinelibrary.wiley.com/doi/abs/10.1029/2019JD030693 doi: https://doi.org/10.1029/2019JD030693

da Silva, C. L., Winn, W. P., Taylor, M. C., Aulich, G. D., Hunyady, S. J., Eack, K. B., ... Trueblood, J. J. (2023). Polarity asymmetries in rocket-triggered lightning. *Geophysical Research Letters*, *50*(17), e2023GL105041. Retrieved from https://agupubs.onlinelibrary.wiley.com/doi/abs/10.1029/2023GL105041 (e2023GL105041 2023GL105041) doi: https://doi.org/10.1029/2023GL105041

Ding, Z., Rakov, V. A., Zhu, Y., Kereszy, I., Chen, S., & Tran, M. D. (2024). Propagation mechanism of branched downward positive leader resulting in a negative cloud-to-ground flash. *Journal of Geophysical Research: Atmospheres*, *129*(1), e2023JD039262. Retrieved from https://agupubs.onlinelibrary.wiley.com/doi/abs/10.1029/2023JD039262 (e2023JD039262 2023JD039262) doi: https://doi.org/10.1029/2023JD039262

Edens, H. E., Eack, K. B., Rison, W., & Hunyady, S. J. (2014). Photographic observations of streamers and steps in a cloud-to-air negative leader. *Geophysical Research Letters*, *41*(4), 1336-1342. Retrieved from https://agupubs.onlinelibrary.wiley.com/doi/abs/10.1002/2013GL059180 doi: https://doi.org/10.1002/2013GL059180

Födisch, P., Wohsmann, J., Lange, B., Schönherr, J., Enghardt, W., & Kaever, P. (2016). Digital high-pass filter deconvolution by means of an infinite impulse response filter. *Nuclear Instruments and Methods in Physics Research Section A: Accelerators, Spectrometers, Detectors and Associated Equipment*, *830*, 484-496. Retrieved from https://www.sciencedirect.com/science/article/pii/S0168900216305617 doi: https://doi.org/10.1016/j.nima.2016.06.019

Gao, Y., Chen, M., Lyu, W., Qi, Q., Qin, Z., Du, Y.-p., & Zhang, Y. (2020). Leader charges, currents, ambient electric fields, and space charges along downward positive leader paths retrieved from ground measurements in metropolis.

Journal of Geophysical Research: Atmospheres, *125*(19), e2020JD032818. Retrieved from https://agupubs.onlinelibrary.wiley.com/doi/abs/10.1029/2020JD032818 (e2020JD032818 2020JD032818) doi: https://doi.org/10.1029/2020JD032818

Hare, B. M., Scholten, O., Buitink, S., Dwyer, J., Liu, N., Sterpka, C., & Veen, S. T. (2023b). Vhf emitting width and 3d polarization of lightning dart leaders. In *2023 xxxvth general assembly and scientific symposium of the international union of radio science (ursi gass)* (p. 1-4). doi: 10.23919/URSIGASS57860.2023.10265623

Hare, B. M., Scholten, O., Buitink, S., Dwyer, J. R., Liu, N., Sterpka, C., & ter Veen, S. (2023a, Jan). Characteristics of recoil leaders as observed by lofar. *Phys. Rev. D*, *107*, 023025. Retrieved from https://link.aps.org/doi/10.1103/PhysRevD.107.023025 doi: 10.1103/PhysRevD.107.023025

Hare, B. M., Scholten, O., Ťureková, P., Cummer, S., Dwyer, J., Liu, N., ... ter Veen, S. (2024, April). Lofar observations of the initial stage of ic dart leaders. In *Egu general assembly 2024* (p. EGU24-7940). Vienna, Austria. doi: https://doi.org/10.5194/egusphere-egu24-7940

Heckman, S. (1992). *Why does a lightning flash have multiple strokes?* (Unpublished doctoral dissertation). Massachusetts Institute of Technology.

Jackson, J. D. (2000, 09). Charge density on thin straight wire, revisited. *American Journal of Physics*, *68*(9), 789-799. Retrieved from https://doi.org/10.1119/1.1302908 doi: 10.1119/1.1302908

Jensen, D. P., Shao, X.-M., & Sonnenfeld, R. (2023a). *Data and Supplementary Material for "Insights into Lightning K-Leader Initiation and Development from Three Dimensional Broadband Interferometric Observations" by Jensen et al.* Zenodo. Retrieved from https://doi.org/10.5281/zenodo.8213032 ([Dataset]) doi: 10.5281/zenodo.8213032

Jensen, D. P., Shao, X.-M., & Sonnenfeld, R. G. (2023b). Insights into lightning k-leader initiation and development from three dimensional broadband interferometric observations. *Journal of Geophysical Research: Atmospheres*, *128*(23), e2023JD039104. Retrieved from https://agupubs.onlinelibrary.wiley.com/doi/abs/10.1029/2023JD039104 (e2023JD039104 2023JD039104) doi: https://doi.org/10.1029/2023JD039104

Jensen, D. P., Sonnenfeld, R. G., Stanley, M. A., Edens, H. E., da Silva, C. L., & Krehbiel, P. R. (2021). Dart-leader and k-leader velocity from initiation site to termination time-resolved with 3d interferometry. *Journal of Geophysical Research: Atmospheres*, e2020JD034309. Retrieved from https://agupubs.onlinelibrary.wiley.com/doi/abs/10.1029/2020JD034309 doi: https://doi.org/10.1029/2020JD034309

Karunarathne, S., Marshall, T. C., Stolzenburg, M., Karunarathna, N., & Orville, R. E. (2015). Modeling stepped leaders using a time-dependent multipole model and high-speed video data. *Journal of Geophysical Research: Atmospheres*, *120*(6), 2419-2436. Retrieved from https://agupubs.onlinelibrary.wiley.com/doi/abs/10.1002/2014JD022679 doi: https://doi.org/10.1002/2014JD022679

Kasemir, H. W. (1960). A contribution to the electrostatic theory of a lightning discharge. *Journal of Geophysical Research (1896-1977)*, *65*(7), 1873-1878. Retrieved from https://agupubs.onlinelibrary.wiley.com/doi/abs/10.1029/JZ065i007p01873 doi: https://doi.org/10.1029/JZ065i007p01873

King, L. (1962). The voltage gradient of the free burning arc in air or nitrogen. *Ionization Phenomena in Gases, Volume I*, 871.

Kolmašová, I., Scholten, O., Santolík, O., Hare, B., Zacharov, P., Lán, R., ... Dwyer, J. (2023). A strong pulsing nature of negative intracloud dart leaders accompanied by regular trains of microsecond-scale pulses. *Geophysical Research Letters*, *50*(10), e2023GL103864. Retrieved from https://

agupubs.onlinelibrary.wiley.com/doi/abs/10.1029/2023GL103864 (e2023GL103864 2023GL103864) doi: https://doi.org/10.1029/2023GL103864

Levenberg, K. (1944). A method for the solution of certain non-linear problems in least squares. *Quarterly of applied mathematics*, *2*(2), 164–168. doi: https://doi.org/10.1090/qam/10666

Lu, G., Winn, W. P., & Sonnenfeld, R. G. (2011). Charge transfer during intracloud lightning from a time-dependent multidipole model. *Journal of Geophysical Research: Atmospheres*, *116*(D3). Retrieved from https://agupubs.onlinelibrary.wiley.com/doi/abs/10.1029/2010JD014495 doi: https://doi.org/10.1029/2010JD014495

Marquardt, D. W. (1963). An algorithm for least-squares estimation of nonlinear parameters. *Journal of the Society for Industrial and Applied Mathematics*, *11*(2), 431-441. Retrieved from https://doi.org/10.1137/0111030 doi: 10.1137/0111030

Marshall, T. C., Stolzenburg, M., Rust, W. D., Williams, E. R., & Boldi, R. (2001). Positive charge in the stratiform cloud of a mesoscale convective system. *Journal of Geophysical Research: Atmospheres*, *106*(D1), 1157-1163. Retrieved from https://agupubs.onlinelibrary.wiley.com/doi/abs/10.1029/2000JD900625 doi: https://doi.org/10.1029/2000JD900625

Mazur, V. (2016). The physical concept of recoil leader formation. *Journal of Electrostatics*, *82*, 79–87. Retrieved from https://www.sciencedirect.com/science/article/pii/S0304388616300407 doi: https://doi.org/10.1016/j.elstat.2016.05.005

Mazur, V., & Ruhnke, L. H. (1993). Common physical processes in natural and artificially triggered lightning. *Journal of Geophysical Research: Atmospheres*, *98*(D7), 12913-12930. Retrieved from https://agupubs.onlinelibrary.wiley.com/doi/abs/10.1029/93JD00626 doi: https://doi.org/10.1029/93JD00626

Mazur, V., & Ruhnke, L. H. (1998). Model of electric charges in thunderstorms and associated lightning. *Journal of Geophysical Research: Atmospheres*, *103*(D18), 23299-23308. Retrieved from https://agupubs.onlinelibrary.wiley.com/doi/abs/10.1029/98JD02120 doi: https://doi.org/10.1029/98JD02120

Mazur, V., & Ruhnke, L. H. (2014). The physical processes of current cutoff in lightning leaders. *Journal of Geophysical Research: Atmospheres*, *119*(6), 2796–2810.

Mazur, V., Ruhnke, L. H., & Laroche, P. (1995). The relationship of leader and return stroke processes in cloud-to-ground lightning. *Geophysical Research Letters*, *22*(19), 2613-2616. Retrieved from https://agupubs.onlinelibrary.wiley.com/doi/abs/10.1029/95GL02348 doi: https://doi.org/10.1029/95GL02348

Miki, M., Rakov, V. A., Rambo, K. J., Schnetzer, G. H., & Uman, M. A. (2002). Electric fields near triggered lightning channels measured with pockels sensors. *Journal of Geophysical Research: Atmospheres*, *107*(D16), ACL 2-1-ACL 2-11. Retrieved from https://agupubs.onlinelibrary.wiley.com/doi/abs/10.1029/2001JD001087 doi: https://doi.org/10.1029/2001JD001087

Montano, R., Becerra, M., Cooray, V., Rahman, M., & Liyanage, P. (2006). Resistance of spark channels. *IEEE Transactions on Plasma Science*, *34*(5), 1610-1619. doi: 10.1109/TPS.2006.883350

Nag, A., Rakov, V. A., & Cummins, K. L. (2014). Positive lightning peak currents reported by the u.s. national lightning detection network. *IEEE Transactions on Electromagnetic Compatibility*, *56*(2), 404-412. doi: 10.1109/TEMC.2013.2280000

Orville, R. E. (1975). Spectrum of the lightning dart leader. *Journal of Atmospheric Sciences*, *32*(9), 1829 - 1837. Retrieved from https://journals.ametsoc.org/view/journals/atsc/32/9/1520-0469_1975_032_1829_sotldl_2_0_co_2

.xml doi: 10.1175/1520-0469(1975)032⟨1829:SOTLDL⟩2.0.CO;2

Pasko, V. P. (2014). Electrostatic modeling of intracloud stepped leader electric fields and mechanisms of terrestrial gamma ray flashes. *Geophysical Research Letters*, *41*(1), 179-185. Retrieved from https://agupubs.onlinelibrary.wiley.com/doi/abs/10.1002/2013GL058983 doi: https://doi.org/10.1002/2013GL058983

Petersen, D. A., & Beasley, W. H. (2013). High-speed video observations of a natural negative stepped leader and subsequent dart-stepped leader. *Journal of Geophysical Research: Atmospheres*, *118*(21), 12,110-12,119. Retrieved from https://agupubs.onlinelibrary.wiley.com/doi/abs/10.1002/2013JD019910 doi: https://doi.org/10.1002/2013JD019910

Qin, J., & Pasko, V. P. (2014, oct). On the propagation of streamers in electrical discharges. *Journal of Physics D: Applied Physics*, *47*(43), 435202. Retrieved from https://dx.doi.org/10.1088/0022-3727/47/43/435202 doi: 10.1088/0022-3727/47/43/435202

Rakov, V. A. (1998). Some inferences on the propagation mechanisms of dart leaders and return strokes. *Journal of Geophysical Research: Atmospheres*, *103*(D2), 1879-1887. Retrieved from https://agupubs.onlinelibrary.wiley.com/doi/abs/10.1029/97JD03116 doi: 10.1029/97JD03116

Rakov, V. A., Thottappillil, R., & Uman, M. A. (1992). On the empirical formula of willett et al. relating lightning return-stroke peak current and peak electric field. *Journal of Geophysical Research: Atmospheres*, *97*(D11), 11527-11533. Retrieved from https://agupubs.onlinelibrary.wiley.com/doi/abs/10.1029/92JD00720 doi: https://doi.org/10.1029/92JD00720

Rakov, V. A., & Uman, M. A. (2003). *Lightning: physics and effects*. Cambridge university press.

Shao, X.-M., Jensen, D., Ho, C., Graham, P., Haynes, W., Caffrey, M., ... Sonnenfeld, R. (2023). Three-dimensional broadband interferometric mapping and polarization (bimap-3d) observations of lightning discharge processes. *Journal of Geophysical Research: Atmospheres*, *128*(4), e2022JD037955. Retrieved from https://agupubs.onlinelibrary.wiley.com/doi/abs/10.1029/2022JD037955 (e2022JD037955 2022JD037955) doi: https://doi.org/10.1029/2022JD037955

Smith, D. A., Eack, K. B., Harlin, J., Heavner, M. J., Jacobson, A. R., Massey, R. S., ... Wiens, K. C. (2002). The los alamos sferic array: A research tool for lightning investigations. *Journal of Geophysical Research: Atmospheres*, *107*(D13), ACL 5-1-ACL 5-14. Retrieved from https://agupubs.onlinelibrary.wiley.com/doi/abs/10.1029/2001JD000502 doi: https://doi.org/10.1029/2001JD000502

Sonnenfeld, R. G., Battles, J. D., Lu, G., & Winn, W. P. (2006). Comparing e field changes aloft to lightning mapping data. *Journal of Geophysical Research: Atmospheres*, *111*(D20). Retrieved from https://agupubs.onlinelibrary.wiley.com/doi/abs/10.1029/2006JD007242 doi: https://doi.org/10.1029/2006JD007242

Sonnenfeld, R. G., Jensen, D. P., Contreras-Vidal, L., Pantuso, J., daSilva, C. L., Clonch, C., ... Edens, H. E. (2023). Detailed streamer observations & modeling of a nearby negative flash. *Authorea Preprints*. Retrieved from https://essopenarchive.org/doi/full/10.22541/essoar.170240442.22551037

Stolzenburg, M., & Marshall, T. C. (2008). Charge structure and dynamics in thunderstorms. *Space Science Reviews*, *137*, 355–372. doi: https://doi.org/10.1007/s11214-008-9338-z

Stolzenburg, M., Marshall, T. C., Karunarathne, S., Karunarathna, N., & Orville, R. E. (2015). Transient luminosity along negative stepped leaders in lightning. *Journal of Geophysical Research: Atmospheres*, *120*(8), 3408-3435. Retrieved from https://agupubs.onlinelibrary.wiley.com/doi/abs/

10.1002/2014JD022933 doi: https://doi.org/10.1002/2014JD022933

Stolzenburg, M., Marshall, T. C., Rust, W. D., Bruning, E., MacGorman, D. R., & Hamlin, T. (2007). Electric field values observed near lightning flash initiations. *Geophysical Research Letters*, *34*(4). Retrieved from https://agupubs.onlinelibrary.wiley.com/doi/abs/10.1029/2006GL028777 doi: https://doi.org/10.1029/2006GL028777

Uman, M. A., & Voshall, R. E. (1968). Time interval between lightning strokes and the initiation of dart leaders. *Journal of Geophysical Research (1896-1977)*, *73*(2), 497-506. Retrieved from https://agupubs.onlinelibrary.wiley.com/doi/abs/10.1029/JB073i002p00497 doi: https://doi.org/10.1029/JB073i002p00497

Willett, J. C., Bailey, J. C., Idone, V. P., Eybert-Berard, A., & Barret, L. (1989). Submicrosecond intercomparison of radiation fields and currents in triggered lightning return strokes based on the transmission-line model. *Journal of Geophysical Research: Atmospheres*, *94*(D11), 13275-13286. Retrieved from https://agupubs.onlinelibrary.wiley.com/doi/abs/10.1029/JD094iD11p13275 doi: https://doi.org/10.1029/JD094iD11p13275

Wolfram Research Inc. (2024). *Wolfram|Alpha.* Wolfram Research, Inc. Retrieved from https://www.wolframalpha.com (Champaign, IL, 2024)

Yos, J. M. (1963). *Transport properites of nitrogen, hydrogen, oxygen, and air to 30,000 k.* Clearinghouse for Federal Scientific and Technical Information.

Zhang, J. (2010). *Development and test of the langmuir electric field array* (Unpublished master's thesis). New Mexico Institute of Mining and Technology.